Results in Engineering 28 (2025) 107619

Contents lists available at ScienceDirect

Results in Engineering

journal homepage: www.sciencedirect.com/journal/results-in-engineering

Research paper

2D/2D N-doped reduced graphene oxide/hexagonal boron nitride composites from recycled batteries for high-performance symmetric coil cell supercapacitors

Yogapriya Selvaraj [a], Nandhakumar Eswaramoorthy [b,*], Vijayakumar Elayappan [c], Prem Kumar Muthusamy [d], Anbazhagan Venkattappan [a], Kiruthika Paramasivam [e], Mohamed Mussa Mtangi [f], Sambasivam Sangaraju [g,*]

[a] Department of Chemistry, Vinayaka Mission's Kirupananda Variyar Arts & Science College, Vinayaka Mission's Research Foundation Deemed to be University, Salem 636308, Tamil Nadu, India
[b] Centre for Applied Nanomaterials, Chennai Institute of Technology, Chennai 600 069, Tamil Nadu, India
[c] Advanced Energy Materials R&D Division, Dongkwang Co.Ltd., Anyang-si, Gyeonggi-do, 14057, South Korea
[d] Department of Mechanical Engineering, Kangeyam Institute of Technology, Tiruppur 638 108, Tamil Nadu, India
[e] Materials Research and Product Laboratory, Department of Chemistry, Coimbatore Institute of Technology, Coimbatore 641014, India
[f] Department of Physics, University of Dar es Salaam, P.O. Box 35063, Dar es Salaam, Tanzania
[g] National Water and Energy Center, United Arab Emirates University, Al Ain, 15551, United Arab Emirates

ARTICLE INFO

Keywords:
Spent battery
N-doped reduced graphene oxide
Boron nitride
2D/2D hybrid composites
Coin cell supercapacitor
LED light applications

ABSTRACT

The growing demand for energy storage solutions has necessitated the development of advanced materials with high efficiency, sustainability, and cost-effectiveness. This study explores the recycling of waste batteries into nitrogen-doped reduced graphene oxide (N-RGO) incorporated with boron nitride (BN) nanosheets for supercapacitor applications. The synthesis process involves a sustainable Electrochemical Exfoliation, Modified Hummer's and simple sonication methods which enabling the recovery of valuable carbon-based materials from waste batteries and their functionalization with nitrogen. Electrochemical analysis of N-RGO/BN composite shows excellent specific capacitance and lower charge transfer resistance for three electrode configurations. In full cell, the device achieved excellent specific capacitance of 86 F g^{-1}, specific energy of 12 Wh kg^{-1} and specific power of 200 W kg^{-1} with capacitance retention of 88 % and 95 % of coulombic efficiency even after 10,000 cycles in coin cell configuration. The results highlight the potential of recycling waste batteries into functional materials for sustainable energy storage systems, contributing to both environmental preservation and technological advancement.

1. Introduction

In recent years, growing concerns about global warming and the depletion of fossil fuel reserves have driven researchers to seek renewable and sustainable energy storage solutions [1]. Among the commonly utilized energy storage systems, rechargeable batteries, such as lithium-ion and sodium-ion batteries, and electrochemical capacitors, particularly electrochemical double-layer capacitors (EDLCs), are regarded as viable candidates for meeting future energy demands [2–5]. However, despite their widespread use, rechargeable batteries face limitations such as low power density, prolonged charging/discharging times, high maintenance requirements, and relatively short lifespans [6,7]. Recycling waste batteries into carbon-based materials for supercapacitor applications offers a sustainable solution to environmental and energy challenges. It reduces hazardous waste, promotes resource recovery, and supports a circular economy by repurposing valuable components like carbon [8]. This approach provides a cost-effective method for producing advanced materials, such as nitrogen-doped reduced graphene oxide, which enhances the performance of supercapacitors. By improving energy density, cycle stability, and conductivity, recycled materials contribute to efficient and durable energy storage systems, aligning with renewable energy goals while reducing

* Corresponding authors.
E-mail addresses: nandhumech01@gmail.com (N. Eswaramoorthy), s_sambasivam@uaeu.ac.ae (S. Sangaraju).

https://doi.org/10.1016/j.rineng.2025.107619
Received 22 June 2025; Received in revised form 15 September 2025; Accepted 7 October 2025
Available online 8 October 2025

reliance on raw material extraction and lowering production costs [9, 10].

Carbon-based materials, including activated carbon, carbon nanotubes, carbon nanofibers, and graphene, have long been recognized as essential electrode materials for supercapacitor applications due to their superior conductivity, high surface area, and chemical stability. Among these, reduced graphene oxide (RGO) has emerged as a standout material, offering exceptional properties and versatility for energy storage systems. As a derivative of graphene, RGO combines a large surface area and excellent electrical conductivity, both of which are crucial for optimizing charge storage and enabling rapid ion transport. Additionally, its partially reduced structure retains residual oxygen functional groups that facilitate pseudocapacitance through faradaic redox reactions, thereby augmenting the electric double-layer capacitance (EDLC) mechanism. The tunable chemical composition of RGO further enhances its performance, as it can form synergistic hybrids with materials such as metal oxides, polymers, and heteroatom-doped carbons. This unique combination of properties, coupled with RGO's mechanical flexibility and compatibility with scalable fabrication methods, makes it an ideal candidate for advanced supercapacitors, offering high energy density, remarkable cycling stability, and diverse applications in renewable energy systems and portable electronics [11–15]. RGO has certain inherent limitations, such as a tendency to agglomerate due to van der Waals interactions, which reduces the available surface area for charge storage. Additionally, the presence of residual oxygen functional groups can compromise its conductivity. Moreover, achieving precise control over the extent of reduction and doping during synthesis can be challenging, potentially leading to inconsistent electrochemical performance [16].

To overcome this limitation, heteroatom doping has emerged as a promising strategy, wherein elements such as nitrogen (N), boron (B), sulfur (S), and phosphorus (P) are introduced into the carbon lattice. This approach enhances capacitive properties by introducing additional pseudocapacitance through faradaic reactions between the electrode material and the electrolyte, thereby significantly improving energy storage capabilities [17–19]. Among heteroatom-doped materials, hexagonal boron nitride (h-BN) has garnered considerable interest due to its high thermal stability and unique structural properties. It is particularly valued in nanotechnology applications, such as high-temperature equipment and as a substrate material [20]. However, the inherent insulating nature of pristine h-BN, with a bandgap of approximately 5.5 eV, limits its direct application in energy storage systems. Through strategic modifications like incorporation into composites or doping with conductive elements, h-BN-based materials can unlock new potential for next-generation supercapacitors, combining thermal stability with enhanced electrical properties [21,22].

This paper explores the synthesis, characterization, and electrochemical performance of Nitrogen-doped reduced graphene oxide (N-RGO) incorporated with boron nitride (BN) sheets offers unique advantages for supercapacitor applications by combining the high conductivity of N-RGO with the stability and mechanical strength of BN. The introduction of nitrogen atoms into the graphene lattice enhances its surface polarity, active sites, and pseudocapacitive behavior, thereby improving charge storage capabilities. Simultaneously, the incorporation of BN sheets mitigates aggregation issues in graphene, increases the electrode's thermal and chemical stability, and provides synergistic effects due to the interaction between graphene's electronic properties and BN's structural characteristics. This hybrid material enables high capacitance, excellent rate capability, and long cycle life, making it a promising candidate for next-generation energy storage systems The objective of the work is represented in **scheme S1**.

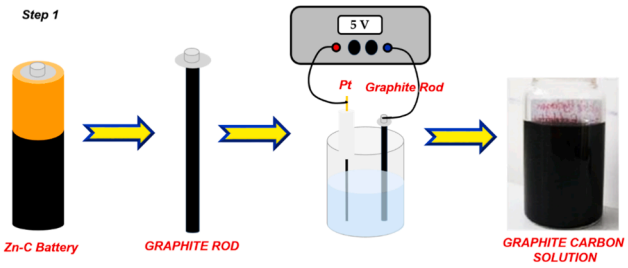

Scheme 1. Schematic representation of the electrochemical exfoliation GO solution preparation.

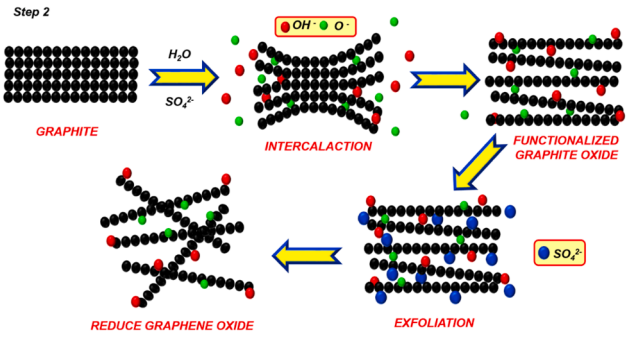

Scheme 2. Schematic representation of the GO to rGO formation.

2. Material and methods

2.1. Materials

Hexagonal boron nitride (h-BN, 1 μm size), purchased from Merck, India. Potassium permanganate ($KMnO_4$, 99 %), Sodium hydroxide (98 %), Sulfuric acid (H_2SO_4, 98 %), Hydrogen peroxide (H_2O_2), Ammonium Sulfate $(NH_4)_2SO_4$, hydrazine hydrate was bought from Sigma, India. All the experimental work conducted by utilizing for double distilled (DD) water.

2.2. Preparation of graphene by electrochemical exfoliation method

Electrochemical exfoliation of graphite was conducted in a two-electrode system, using a platinum counter electrode and a graphite flake as the working electrode. The aqueous inorganic salt electrolytes tested, sulfate-containing salts such as $(NH_4)_2SO_4$ showed the highest exfoliation fficiency. A 0.1 M $(NH_4)_2SO_4$ solution with neutral pH was prepared as the electrolyte. When a direct current (DC) voltage of +5 V was applied, the graphite flakes began to dissociate and disperse into the electrolyte within 3–5 min. The exfoliated material was collected via vacuum filtration, washed thoroughly to remove residual salts. The exfoliated powder was dispersed in DMF by sonication for 10 min, resulting powder was collected and used for further process. Scheme 1 and 2 represents the electrochemical exfoliation method.

2.3. Preparation of graphene oxide by modified Hummer's method

The next step involves preparing graphite oxide (GO) through an oxidation process. Three grams of the cleaned graphite rods are placed in a beaker and mixed with 60 mL of concentrated sulfuric acid (H_2SO_4), added slowly while stirring, ensuring the temperature remains below 20 °C. Potassium permanganate (2 g of $KMnO_4$) is gradually introduced into the mixture under the same temperature conditions, followed by stirring for two hours at room temperature. Afterward, 120 mL of distilled water is added cautiously to dilute the reaction, which may become exothermic. Stirring is continued for another hour before 10 mL

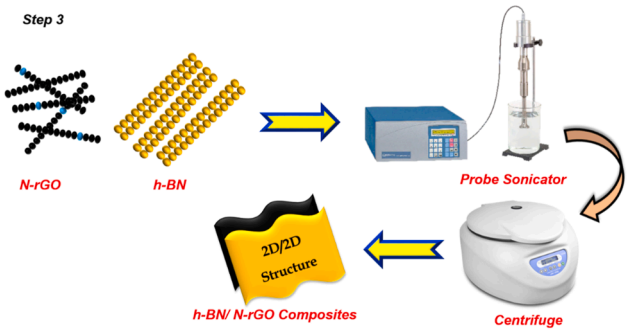

Scheme 3. Schematic representation of the 2D/2D structured h-BN/N-RGO composites (ultra-sonication method).

of hydrogen peroxide (H_2O_2) is added to terminate the oxidation, turning the mixture bright yellow or light brown, indicating the formation of graphite oxide. The product is then filtered, washed with distilled water and ethanol until the filtrate reaches a neutral pH, and dried in a vacuum oven at 60 °C for 12 h.

2.4. Preparation of N-doped reduced graphene oxide (N-RGO)

Reduction of the graphene oxide to RGO follows by dispersing the GO in 100 mL of distilled water and adding a reducing agent (hydrazine hydrate). The solution is stirred at 80 °C for two hours, during which a color change to black indicates successful reduction. The reduced graphene oxide is filtered, washed with distilled water and ethanol to remove residual reducing agents, and dried in a vacuum oven at 60 °C for 12 h.

2.5. Ultrasonic assisted h-BN/ 1, 3, 5 and 10 wt. % N-RGO composites preparation

To synthesize 1, 3, 5 and 10 wt. % of N-doped reduced graphene oxide (N-RGO) doped with hexagonal boron nitride composites via a simple sonication method, the process begins with mixing of N-RGO and BN. A hexagonal boron nitride (h-BN) suspension is gradually added to the 100 mL water and various wt. % of N-RGO suspension was added, and the mixture is stirred for 15 min to promote initial interactions between N-RGO and h-BN. This is followed by ultrasonication of the combined suspension for 1 h to ensure proper mixing and uniform distribution of h-BN within the N-RGO matrix. During this step, strong interactions, such as van der Waals forces or π-π interactions, form between the two materials. After sonication, the mixture is stirred for an additional 3 h to stabilize the composite. The stabilized suspension is then filtered to separate the N-RGO/h-BN composite. It is thoroughly washed with distilled water and ethanol to remove any unreacted materials or impurities. Finally, the resulting composite is dried in a vacuum oven at 60 °C for 12 h, yielding the N-RGO/h-BN composite with excellent properties for advanced applications (Scheme 3).

2.6. Preparation of electrode

In electrochemical characterization, the three electrode configurations, the prepared materials act as working electrode, Ag/AgCl act as reference electrode and platinum wire act as counter electrode. The working electrode is prepared by drop-casting method using 80:10:10 ratio of active material, polyvinylidene fluoride (PVDF as binder) and acetylene black were mixing with NMP solvent until it became a fine paste. The mixture was coated on 1 × 1 cm of graphite sheet substrate and it heated at 60 °C for 12 h for evaporating the solvents and removal of other impurities. Then heated electrode were cooled down to room temperature. The total active mass is ~1 mg then the electrode was used to electrochemical analysis. The potential range of 0.0 to 0.8 V was maintained for cyclic voltammetry (CV) and galvanostatic charging–discharging (GCD) analysis to avoid the overpotential of water. Electrochemical impedance spectroscopy (EIS) was carried out in the 1 MHz to 1 Hz frequency range at room temperature. For the half-cell test the specific capacitance were calculated by Eq. (1) and 2 from CV analysis and GCD analysis,

$$C_{sp} = \frac{\int IdV}{2m\nu\Delta V}\left(\mathrm{Fg}^{-1}\right)(\mathrm{FromCVAnalysis}) \tag{1}$$

$$C_{sp} = \frac{I \times \Delta t}{m \times \Delta V}\left(\mathrm{Fg}^{-}\right)(\mathrm{FromGCDAnalysis}) \tag{2}$$

From the equation, Csp represents the specific capacitance (F g^{-1}), ∫ IdV is integrated area of total charge corresponding to potential window, ν for scan rate (mV s^{-1}), m denotes mass of active material (g), V for potential window (V), I is discharging current density (A g^{-1}), and t is discharging time (s) [23–25].

In the full cell test, a symmetric device was fabricated using 80:10:10 ratio of 10 % N-RGO/BN as the active material, PVDF as binder and carbon black as conductive additive for both the positive and negative electrodes. The mixture was converted into fine paste using suitable solvent to create a uniform slurry. The slurry is then coated onto a conductive graphite sheet substrate, and dried at elevated temperatures to remove solvents. The dried electrodes are punched into circular disks and assembled in coin cell casings with a porous Whatman filter paper as separator and 3 M KOH as electrolyte. The components are carefully stacked, sealed using a crimping machine for airtightness, and subjected to electrochemical testing such as cyclic voltammetry, charge-discharge cycles, and impedance spectroscopy to evaluate performance. This process ensures reliable assembly and testing of supercapacitor devices. The device capacitance (C_D), specific energy (E), specific power (P) and coulombic efficiency (η) are calculated by following equations,

$$\textit{Device capacitance}\ (C_D) = 4\frac{I \times \Delta t}{m \times \Delta V}\ \left(\mathrm{F\ g}^{-1}\right) \tag{3}$$

$$\textit{Spefic Energy}\ (E) = \frac{1}{2} \times C_D \times (\Delta V)^2 \times \frac{1}{3.6}\ \left(\mathrm{Wh\ kg}^{-1}\right) \tag{4}$$

$$\textit{Specific Power}\ (P) = \frac{E \times 3600}{\Delta t}\ \left(\mathrm{W\ kg}^{-1}\right) \tag{5}$$

$$\textit{Coulombic Efficiency}\ (\eta) = \frac{\Delta t_D}{\Delta t_C} \times 100\% \tag{6}$$

2.7. Characterization techniques

The absorbance properties of the composite were analyzed using ultraviolet-visible (UV–Vis) spectroscopy (JASCO V-670 PC). The crystalline nature of the h-BN and h-BN/N-RGO composites are analyzed using X-ray diffraction (XRD) using an X-ray diffractometer (XRD) with Cu-Kα radiation (Ultima IV, Rigaku), with the 2θ range of 5° to 80° The oxidation state and elemental composition of the as synthesized samples were analyzed by X-ray photoelectron spectroscopy (XPS, PHI 5000 VersaProbe III, Physical Electronics). The structural and surface morphology analyzed using field emission scanning electron microscope (FE-SEM) (SIGMA HD, Carl Zeiss Microscopy). The intrinsic surface morphology images are analysed by high resolution transmission electron microscope (HR-TEM) (JEOL, JEM 2100Plus). All electrochemical measurements were conducted using the CH Instrument (CHI 6087E) electrochemical analyzer. For cyclic voltammetry (CV) and galvanostatic charge-discharge (GCD) studies. Additionally, electrochemical impedance spectroscopy (EIS) was performed across a frequency range of 1 Hz to 100 kHz, utilizing an AC amplitude of 10 mV. These experimental conditions provide a comprehensive evaluation of the electrochemical properties and performance of the samples.

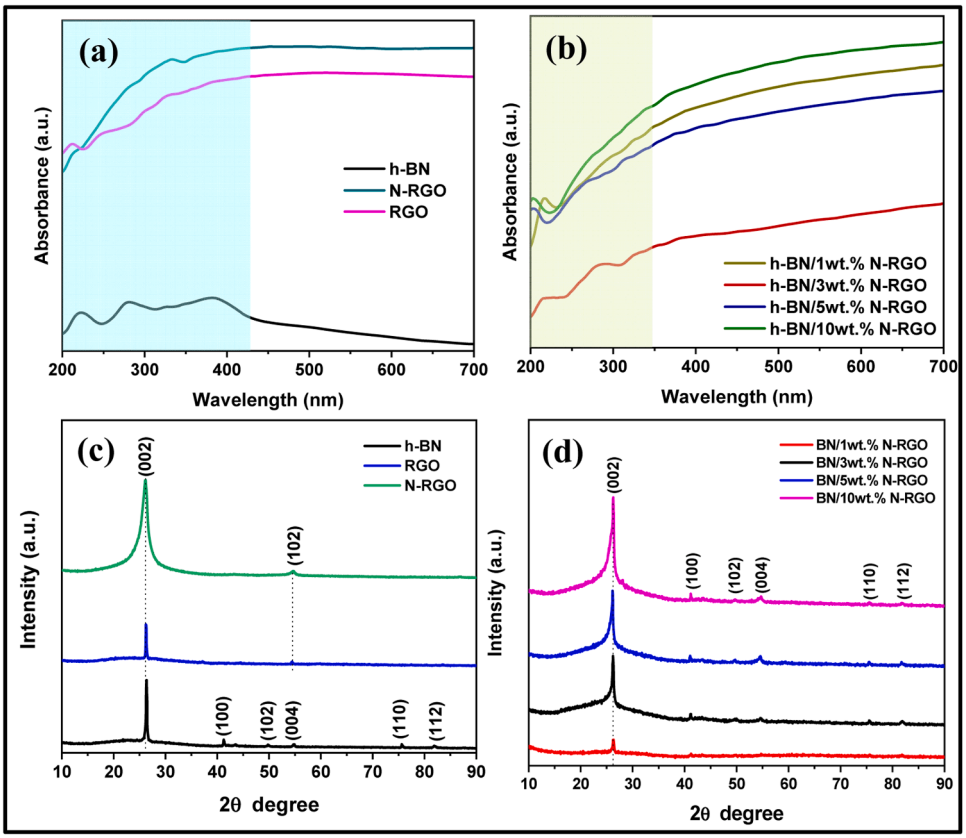

Fig. 1. (a, b) UV–Vis (c, d) XRD analysis of h-BN, RGO, N-RGO, h-BN/1 wt. %N-RGO, h-BN/3 wt. %N-RGO, h-BN/5 wt. %N-RGO and h-BN/10 wt. %N-RGO samples.

3. Result and discussion

3.1. UV–vis analysis

The absorbance properties of synthesized BN, RGO, N-RGO and N-RGO doped BN were analyzed by UV–Vis spectra, as shown in Fig. 1**a, b**. Pure hexagonal boron nitride (h-BN), reduced graphene oxide (RGO), and nitrogen-doped graphene oxide (N-RGO) samples show light absorbance ranging from 200 to 430 nm. Fig. 1**(a)** displays the white-colored pure h-BN nanosheets sample and indicates the three different absorbance peaks, as clearly indicated at 221, 280, and 386 nm absorbance in the UV region [26,27]. It corresponds to 5.61 eV, 4.42 eV, and 3.21 eV, respectively. The shape and structure as change in the electron states and resultantly lead to change in bang gap values are previously reported in Gao et al. [28] On the other hand, band gap values are estimated from the band gap Eq. (7).

$$Band\ gap\ (E_g) = \frac{1240}{\lambda} \tag{7}$$

Hexagonal boron nitride (h-BN) has a theoretical optical band gap value of about 6 eV, which is slightly equivalent to that of pure h-BN samples. This suggests that the dispersion of bandgap energy levels in pure h-BN has increased. Likewise, it was previously reported that hexagonal boron nitride had an optical band gap of 5.51 eV [29]. On the other hand, it exhibits two absorption peaks at 280 and 386 nm, which are due to the optical transitions and the redistribution of h-BN electron-hole density between van Hove singularities of the excited state. As a wide-band gap material, hexagonal boron nitride is transparent in infrared and visible light, while in ultraviolet light it has a strong optical absorption at 221 nm with a strong exaction peak [26,27]. UV–Vis absorbance peaks of carbon materials are very sensitive to sp^2 and sp^3 sites. In addition, The RGO, and N-RGO material absorbance observed at 210, 250, and 330 nm. The first and second peaks corresponding to the π-π* transition of aromatic C—C bonds indicated the restoration of an extensive conjugated framework of sp^2 carbon atoms. Also, the third absorbance peak clearly denoted the *n*-π* transitions of $C = O$ bonds [30]. When the RGO is obtained from GO, the oxygen content decreases, and the transition occurs from sp^3 to sp^2 and changes into the absorbance range as shown in Fig. 1**b,** respectively [31]. Commonly, as the number of sp^2 sites increases, the main absorbance peak shifts towards higher wavelengths (red shift). Conversely, Fig. 1**b** illustrates that the 1, 3, 5, and 10 wt. % N-RGO mixed h-BN composite strongly changed in the absorbance band region at 200–320 nm. These peaks were slightly changed at the h-BN/N-RGO composite due to structural ordering and indicate no restoration of electron conjugation in the composite presented in N-RGO [32,33]. These observations support the effective interfacial charge transition of h-BN/N-RGO composites.

3.2. XRD analysis

The XRD pattern was analyzed to confirm the crystal structure of the prepared nanomaterials. The pure (h-BN, RGO and N-RGO) and nanocomposites (h-BN/1wt % N-RGO, h-BN/3wt % N-RGO, h-BN/7wt % N-RGO and h-BN/10wt % N-RGO) samples XRD results as shown in Fig. 1 **(c, d)**. The h-BN material XRD pattern 2θ values 26.44, 41.21, 43.48, 49.83, 54.78, 75.59, 75.79, 81.84 and 82.10 corresponding to the (002), (100), (102), (004), (110) and (112) h k l planes can be conformed to the graphite like hexagonal boron nitride (h-BN) structure as shown in Fig. 1 **(c)**. These results were well aggregated with standard JCPDS Card No: 34–0421. Moreover, Bragg's law Eq. (1) used to calculate the distance between plates [34,35].

$$d_{hkl} = \frac{\lambda}{2sin\ \theta} \tag{1a}$$

Where, d_{hkl} (nm) represents the distance between the plates, which

Elements	Atomic %	Peak Area (Cps)	Binding Energy (eV)	FWHM (eV)
B 1s	37.04	22014.56	190.28	2.42
C 1s	23.98	14252.22	285.05	3.06
N 1s	30.74	18271.85	398.08	2.51
O 1s	8.24	4896.69	532.17	3.16

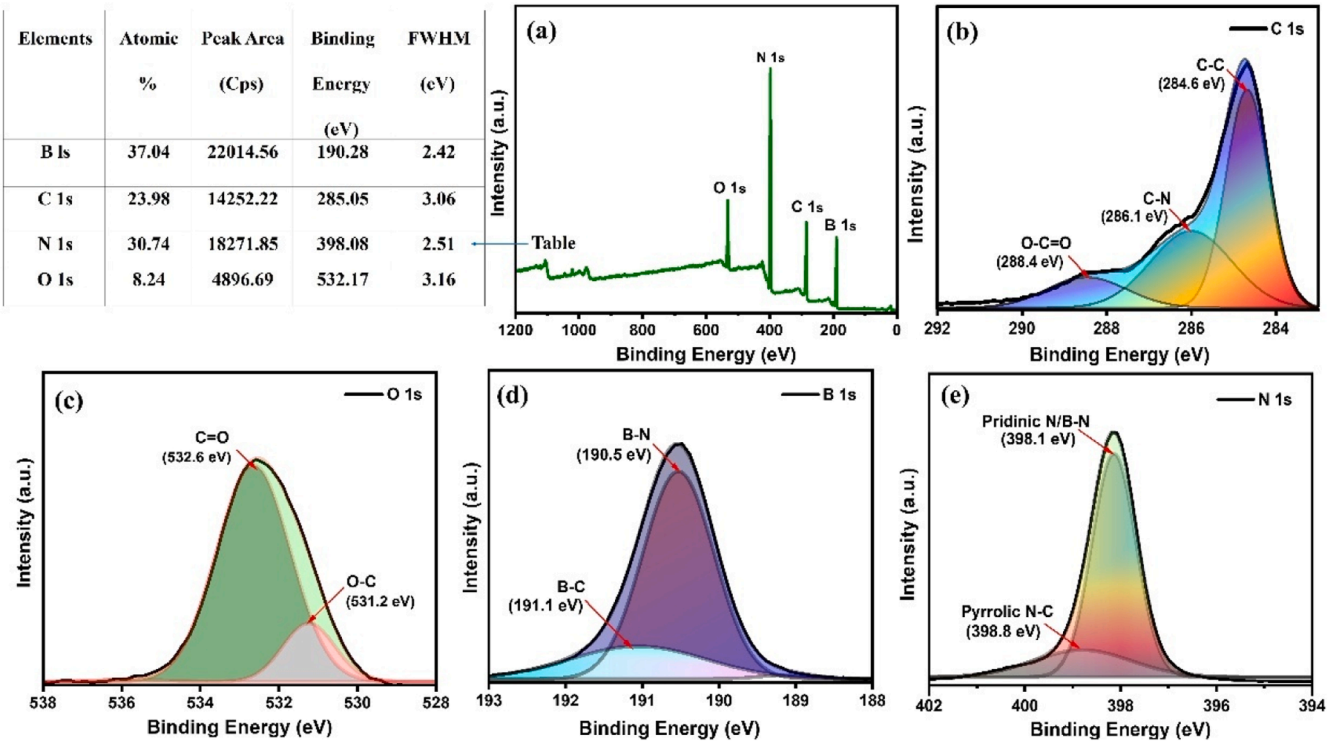

Fig. 2. XPS spectra of h-BN/5 wt. %N-RGO sample (As show in left side element table) (a) Survey spectrum (b) C 1 s (c) O 1 s (d) B 1 s and (e) N 1 s.

corresponding to crystalline plates, θ is the diffraction angles corresponding to the plane (*h k l*). The major 2θ values (22.21°) corresponding to the h k l (002) plan interlayer space (0.336 nm) was strongly confirmed the h-BN plates, which is well consistent with previously reported results [36]. In addition, graphite powder derived the two-dimensional RGO (2θ - 26.25°, 54.41°), and N-RGO (2θ - 26.14°, 54.54°) material 2θ values are well matched with previously reported results [37]. N-RGO samples observed the broad peak due to formation of few layers structured RGO sheets. Comparison of three materials major h k l position corresponding 2θ values was slightly changes was observed; due to interlayer distance it was clearly conformed to the previously reported the XRD results. Moreover, Fig. 1**d** display the h-BN/1 wt. %N-RGO, h-BN/3 wt. %N-RGO h-BN/5 wt. %N-RGO and h-BN/10 wt. %N-RGO samples XRD pattern displayed in the (002), (100), (102), (004), (110) and (112) h k l values are strongly indicated for composites formation. Particularly, a slight increase in peak intensity was observed with increasing N-RGO loading. Additionally, the incorporation of different wt. % of N-RGO into the h-BN material induced stress in the crystal lattice, which was evidenced by a slight shift in the major (002) diffraction plane.

3.3. XPS analysis

The chemical composition and states of prepared h-BN/5 wt. %N-RGO nanocomposite are analyzed by X-ray photoelectron spectroscopy (XPS). The full survey spectrum indicates the presence of boron (B), Oxygen (O), Nitrogen (N) and Carbon (C) elements without impurities are observed in Fig. 2**a** (As show in left side element table). The deconvoluted C 1 s spectrum comprise three prominent peaks located at around 288.4 eV, 286.1 eV and 284.6 eV, respectively, which can be ascribed to O—*C* = *O*, C—N and C—C bonds. The 284.6 eV binding energy corresponding to the C—C (graphitic sp^2 carbon) bonds, which is a validation of the presence of the graphene backbone. In addition, the presence of the sp^2 and sp^3 bonds for the tetrahedral and trigonal phases is observed at 286.1 eV, can be attributed to carbon bonded with nitrogen of h-BN (C—N) as displayed in Fig. 2**b** [38,39].

The peak 288.4 eV is characteristic of the presence of O—*C* = *O* bonds, respectively. Further, the deconvoluted O 1 s spectra, observed at the two major peaks, it's clearly indicated the presence of 531.8 and 532.2 eV binding energies. These are corresponding to O–C (oxygen single bond to carbon) and *C* = *O* (oxygen double bond to aromatic carbon) bonds (See in Fig. 2**c**). These results are accordance with previous reported results [40]. The B 1 s spectrum is shown in Fig. 2**(d)**. The narrow boron peak (B 1 s) was deconvoluted into two major peaks. The major peak located at 190.5 eV and 191.1 eV was corresponding to B-N and B-C bonds of h-BN nanosheets. Similarly, the two major peak was observed in deconvoluted N 1 s spectra as show in Fig. 2e the presence of 398.1 eV and 398.8 eV binding energies, which was matched to pridinic N/B-N and pyrrolic N/N—C bonds. The bonds positions are commonly matched with h-BN and N-RGO material. The N—C and B-N bonds suggesting the h-BN nanosheets attached with N-RGO layer, these are may be similar peak was arrived in the nanocomposites. As observed from the previous literature, the presence of the pyrrolic and pyridinic nitrogen in the core structure of graphene improves its electrical and electrochemical performance during the electrochemical process [41–43].

3.4. FE-SEM, EDX and elemental mapping analysis

The surface morphologies of pure h-BN, RGO and N-RGO samples are shown in **Fig. S1 (a-c)** display the confirmed in the FE-SEM images. The h-BN sample were shown the smooth and layered structure. Moreover, observed the stacked h-BN nanosheets separation are observed in the h-BN surface due to generate the defects in the h-BN lattice. Similarly, modified hummer method treated graphite powder was converted into, RGO and N-RGO layer was illustrate at nanosheets like structure was displayed at different magnification which are shown in **Fig. S1b and c.**

Also, the nanosheets are folded and aggregate morphology was observed in h-BN and RGO samples due to surface charge behavior. These FE-SEM images clearly indicated the tiny stacked layered structure was conformed the formation of few layers thickness nanosheets. It strongly indicated the presence of RGO and it well accordance with

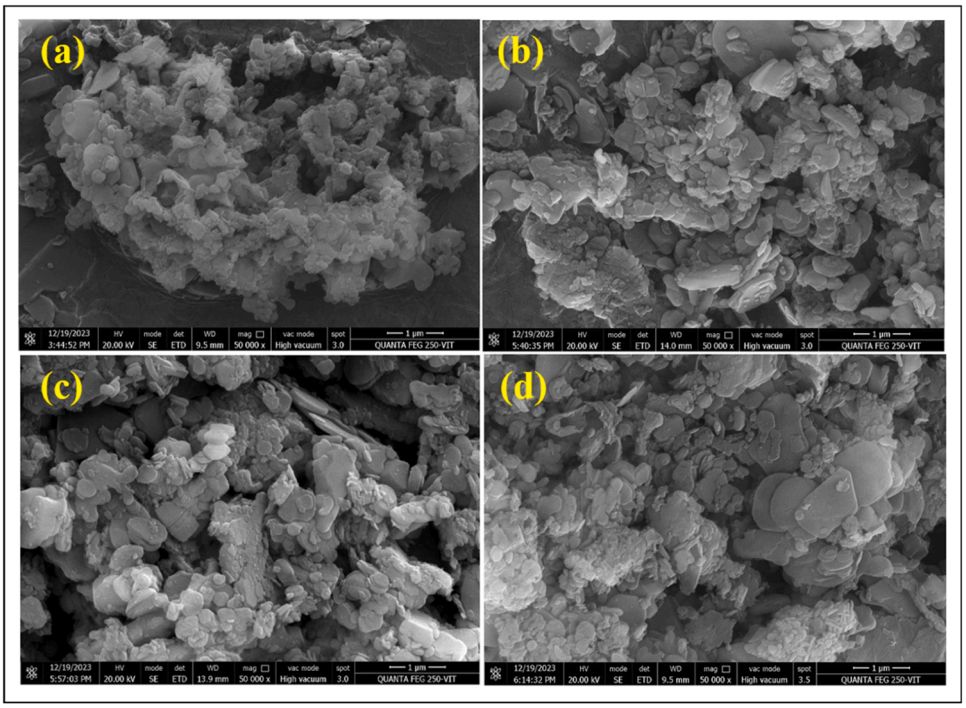

Fig. 3. FE-SEM images of (a) h-BN/1 wt. %N-RGO (b) h-BN/3 wt. %N-RGO (c) h-BN/5 wt. %N-RGO and (d) h-BN/10 wt. %N-RGO samples.

previous reports. Further, hydrothermally treated nitrogen doped reduced graphene oxide (N-RGO) samples was attained at wrinkled, thin-wafer like structure, its clearly observed in the higher magnification FE-SEM images due to N dopant surface functionalized with low temperature condition. In addition, 1, 3, 5 and 10 wt. %N-RGO material mixed with pure h-BN due to it has attained the hybrid nanocomposites structure was illustrated in Fig. 3. The FE-SEM images observed the 1 wt. %N-RGO layer discontinues h-BN surface covered the morphologies was observed at Fig. 3**a**. It clearly confirms the higher magnification FE-SEM images (500 nm scale bar). Further, 3, 5 and 10 wt. % N-RGO material was slowly mixed and layer by layer structure as induced the increase the wt. % of N-RGO which is shown in Fig. 3**b-d**. In Fig. 3**b-d** denotes at aggregated layered structure was observed in the synthesized hybrid composite samples. All these FE-SEM images observed at h-BN nanosheets incorporated with N-RGO and formation of the 2D/2D structured hybrid composites. The prepared sample of h-BN/5 wt. %N-RGO confirms the presence of rich source of Carbon (C), Nitrogen (N), Boron (B) elements are indicated the EDX and elemental mapping analysis. The EDS mapping and EDAX was confirmed the presence of overall elements and individual elements were presence in h-BN/5 wt. %N-RGO sample (22 wt. % of B, 32 wt. % of C, 4.1 wt. % of O and 41.9 wt. % of N) which is shown in **Fig. S2a-f**.

The mapping did not reveal any other elements presented in the hybrid composites. This is in good agreement with the previous reported EDX spectrum results. It has strongly confirmed the purity of synthesized hybrid composites.

3.5. HR-TEM analysis

In order to achieve a deep understanding of the h-BN/5 wt. %N-RGO nanocomposite samples structural nature, lattice fringe and selected area electron diffraction pattern (SAED) are confirmed to the high resolution transmission electron microscopy (HR-TEM) instrument results as shown in Fig. 4. The HR-TEM images exhibit the formation of nanocomposite structure. Moreover, observed h-BN nanosheets surface curtailed-RGO layer was observed in several places in the HR-TEM images as shown in Fig. 4**a, b**. In addition, thin N-RGO and inclined h-BN nanosheets are clearly observed in 200 and 100 nm magnification HR-TEM image. Also, HR-TEM images presented at some dark color was witnessed, that indicated the thick and aggregated nanocomposite or nanosheets formation. It strongly confirms the layer-by-layer (2D/2D) structure formation of h-BN/N-RGO nanosheets was indicated the Fig. 4**c.** This structure can enhance the surface area and facilitate electrolyte charge transport by inhibiting the π–π interactions between the h-BN and N-RGO layers. Moreover, the stacked architecture significantly improved the charge storage capacity of the supercapacitor device. Also, amorphous nature of N-RGO layer as indicated the top of the h-BN nanosheets as clearly revel the 10 nm magnified, HR-TEM image. Also, thin h-BN nanosheets corner surface presented the lattice fringe pattern was observed. In addition, Fig. 4**d** exhibits the h-BN nanosheets surface attached the N-RGO on discontinues places was noticed in the HR-TEM image. The regions marked by the yellow dotted line (indicated in blue) exhibit an amorphous nature, clearly confirming the presence of N-RGO. The lattice fringe ᴅ-spacing of the h-BN nanosheets was determined to be ~0.23 nm, which is in good agreement with previously reported values for h-BN nanosheets [44].

Fig. 4**e** illustrated the h-BN/5 wt. %N-RGO composite sample SAED pattern image, observed the white spots was indicated the crystalline nature of h-BN nanosheets. The observed, SAED pattern formation was not clearly observed due to presented in winkled structured N-RGO covered with h-BN nanosheets surfaces. These are circular shape diffraction spots formation was slightly reduced, due to thickness of h-BN material. Moreover, h-BN nanosheets as a disordered crystal was exhibiting a bright spotted connected circular ring shape diffraction pattern was observed in SAED pattern. These detected bright white spots were well matched with XRD pattern (002), (100), (102), (104), (110) and (112) values were strongly confirmed to h-BN/5 wt. % N-RGO nanocomposites (As show in Fig. 1**d**).

3.6. Electrochemical analysis of 2D/2D structured N-RGO/h-BN hybrid composites

Fig. 5**a-c** shows the cyclic voltammetry curves of h-BN, RGO and N-RGO at the potential window of −0.5 to 0.5 V (vs. Ag/AgCl). Fig. 6**a-**

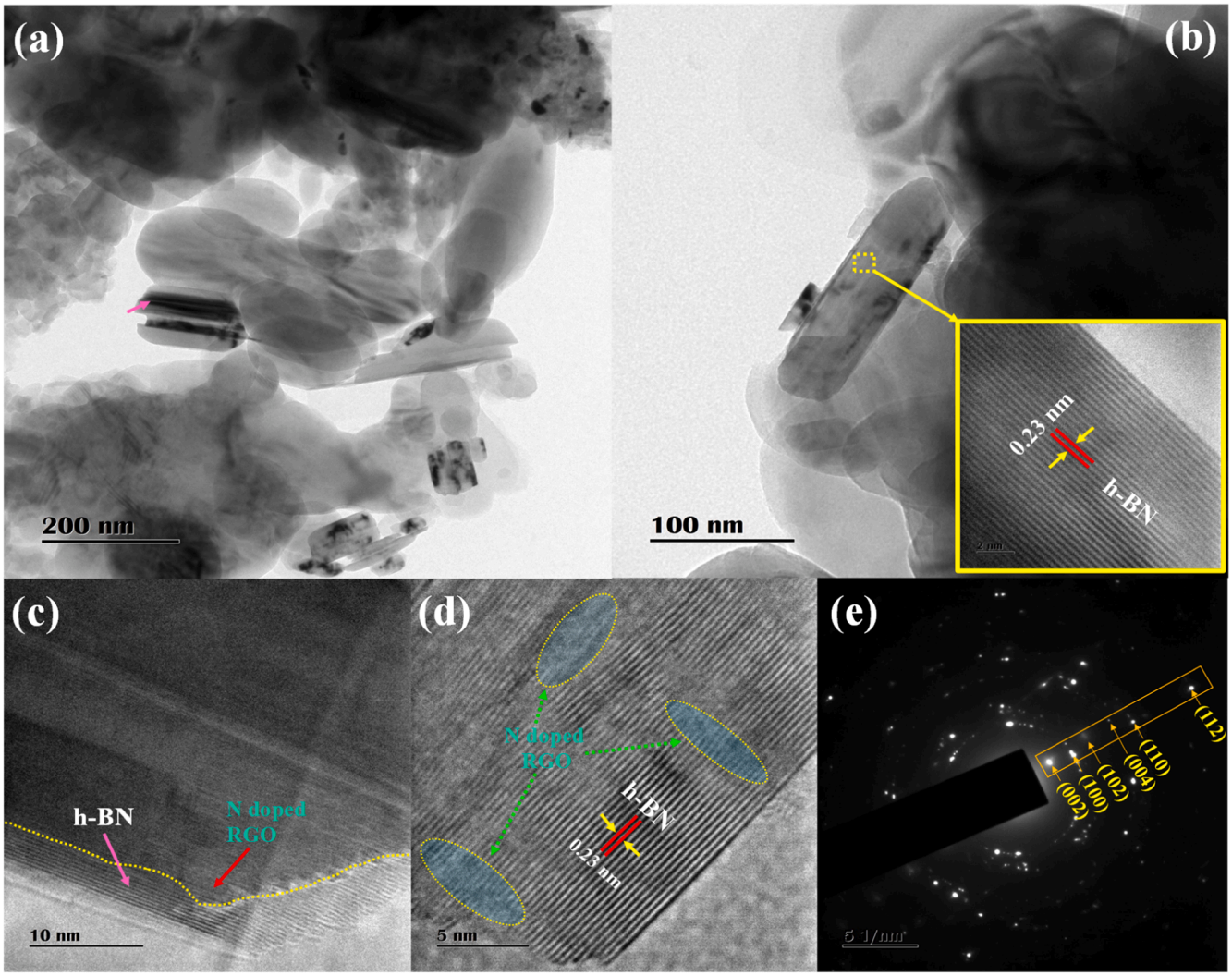

Fig. 4. (a and b) HR-TEM images (c and d) Lattice fringes with various resolution (e) Selected area electron diffraction (SAED) pattern of h-BN/5 wt. %N-RGO sample.

d shows cyclic voltammetry curves of h-BN/N-RGO (1,3, 5 and 10 % N-RGO/ h-BN) composites in 3 M KOH as an electrolyte solution with the potential window of −0.4 to 0.4 V (vs. Ag/AgCl). Prominent oxidation–reduction peaks were observed in h-BN and h-BN/N-RGO composites, which may be due to the ionic bond between boron and nitrogen atoms, and the variable oxidation states of nitrogen.

The oxidation state can change due to intercalation with the electrolytic ions during the redox reaction. On addition of N-RGO, the width of CV curve was gradually increases which maintaining the pseudocapacitive nature for all the h-BN/N-RGO composites. As the scan rate increases, the current response grows proportionally, indicating excellent rate capability and the ability of the material to support rapid charge/discharge cycles [45,46]. The specific capacitance can be calculated from CV curves using Eq. (1), the calculated specific capacitance of h-BN, RGO, N-RGO and h-BN/N-RGO (1,3, 5 and 10 % N-RGO/ h-BN) are 90, 107, 131, 180, 200, 291 and 215 F g^{-1} at the scan rate of 10 mV s^{-1} respectively. The comparison of specific capacitance with respective scan rates for h-BN, RGO, N-RGO shown in Fig. 5**d** and h-BN/N-RGO (1,3, 5 and 10 % N-RGO/ h-BN) shown in Fig. 10**a**. The 5 % N-RGO/ h-BN shows higher specific capacitance than other materials, which represents the optimal concentration for achieving maximum synergy between N-RGO and h-BN, resulting in higher specific capacitance [25]. On doping of higher concentration of 10 % N-RGO/ h-BN shows lower specific capacitance compared to other samples which is due to the stacking of layers and increased faradic resistance. It has been found that RGO contributes to specific capacitance through both EDLC and pseudocapacitance, owing to the presence of residual oxygen functional groups. However, the capacitive nature of RGO deteriorates due to the stacking of GO sheets during reduction. Pure boron nitride has a structure similar to graphite, with conjugated double bonds and free π electrons. These reasons are may reduced the specific capacitance of h-BN, RGO and N-RGO [47,48].

The charge storage mechanism of the 5 % N-RGO/h-BN composite is explained using Dunn's power law. The current response (i_p) at a specific potential (Ag/AgCl) were explained in Eq. (8) and 9,

$$i_p = av^b \tag{8}$$

In this equation, i represents the current (A), a is an adjustable parameter, ν is the scan rate (mV s^{-1}, and b is the slope derived from the logarithmic plot of scan rate (log ν) versus current (log i). The current response is categorized into two mechanisms: diffusion-controlled and surface-controlled. A 'b-value of 1 or higher indicates a surface-controlled mechanism, while a 'b-value of 0.5 or lower signifies a diffusion-controlled mechanism. Intermediate values between 0.5 and 1 suggest contributions from both mechanisms [49–51]. Fig. 7**a** shows the log ν versus log i plot for the 5 % N-RGO/h-BN composite, which exhibits a linear fit. The slope (b-value) is calculated to be 0.82, indicating that the charge storage mechanism is both surface controlled and

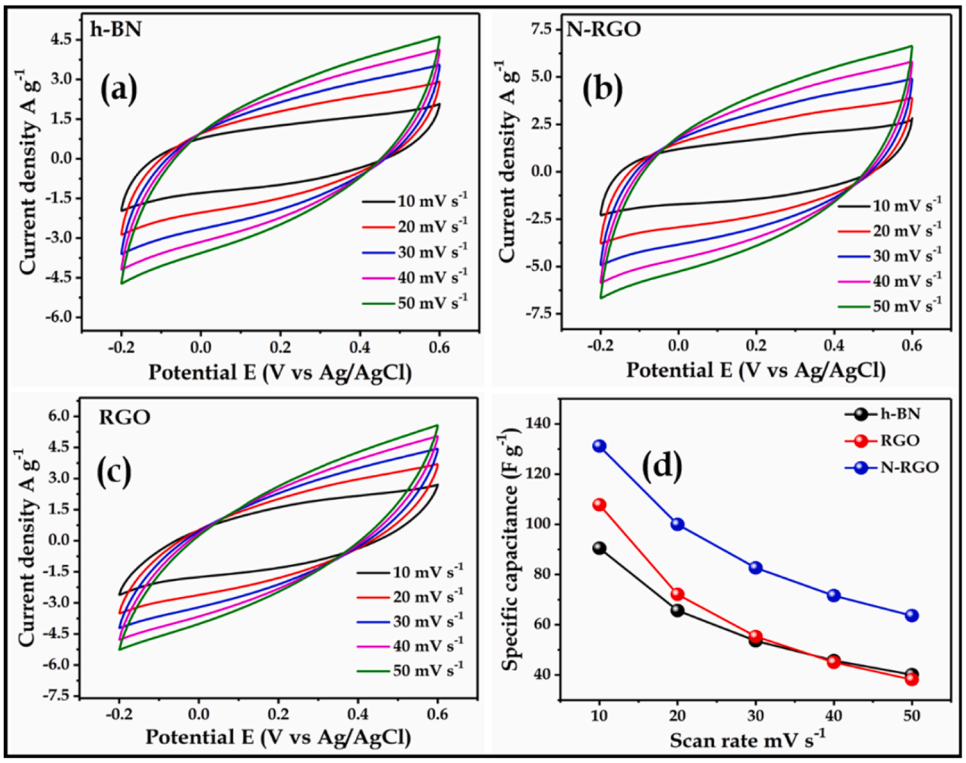

Fig. 5. (a-c) Cyclic voltammetry (CV) curves of h-BN, RGO and N-RGO at scan rates ranging from 10 mV s^{-1} to 50 mV s^{-1}. (d) The relationship between scan rate and specific capacitance for h-BN, RGO and N-RGO.

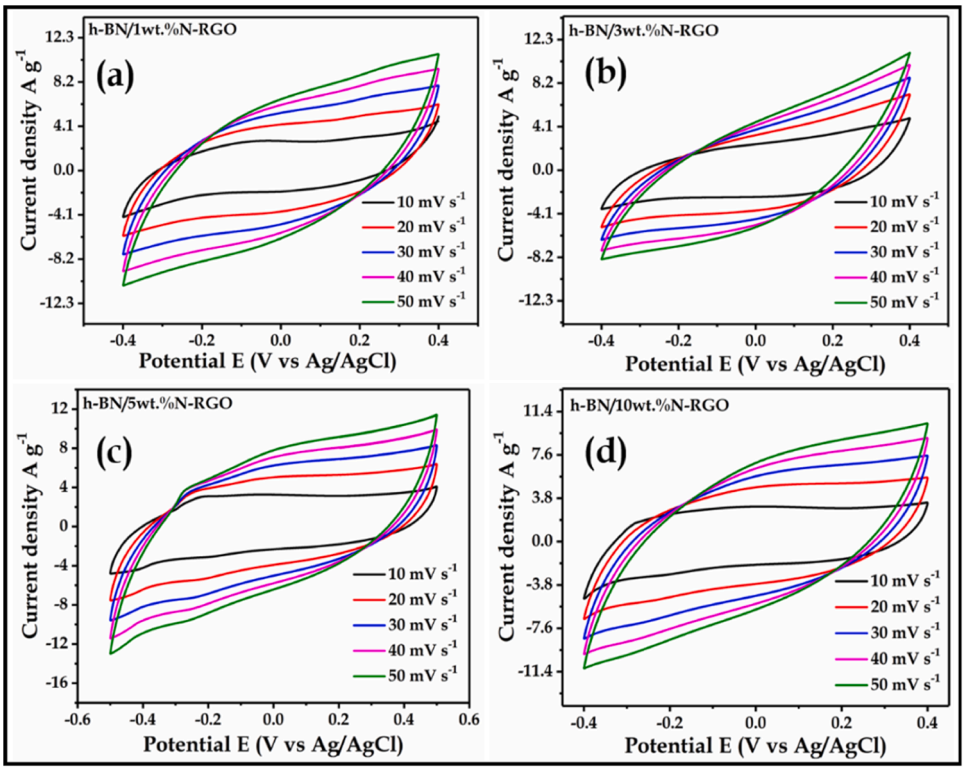

Fig. 6. (a-d) Cyclic voltammetry curves of BN/1 wt. %N-RGO, 1 % N-RGO/ h-BN, 3 % N-RGO/ h-BN and 5 % N-RGO/ h-BN and 10 % N-RGO/ h-BN at scan rate of 10 mV s^{-1} to 50 mV s^{-1}.

diffusion-controlled. The contributions of the surface-controlled and diffusion-controlled mechanisms to the total capacitance are further analyzed using Eq. (8):

$$i_P = k_1 v + k_2 \sqrt{v} \quad (9)$$

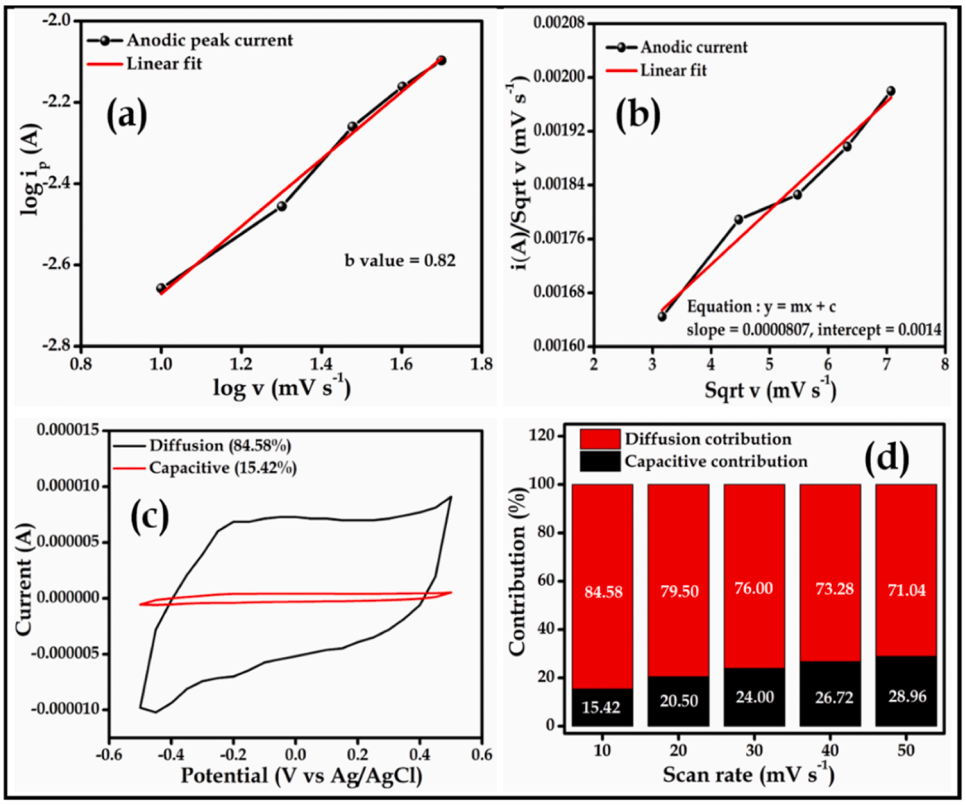

Fig. 7. Charge Storage mechanism of 5 % N-RGO/ h-BN composite. (a) A plot of the logarithm of scan rate (log ν) versus the logarithm of current (log i). (b) A plot of the square root of scan rate (mV s^{-1}) versus anodic current normalized by the square root of scan rate ($i_p/\sqrt{\nu}$). (c) The contributions of diffusion-controlled and capacitive mechanisms at a scan rate of 10 mV s^{-1} (d) The bar diagram for diffusion and capacitive contribution at scan rate between 10 mV s^{-1} to 50 mV s^{-1}.

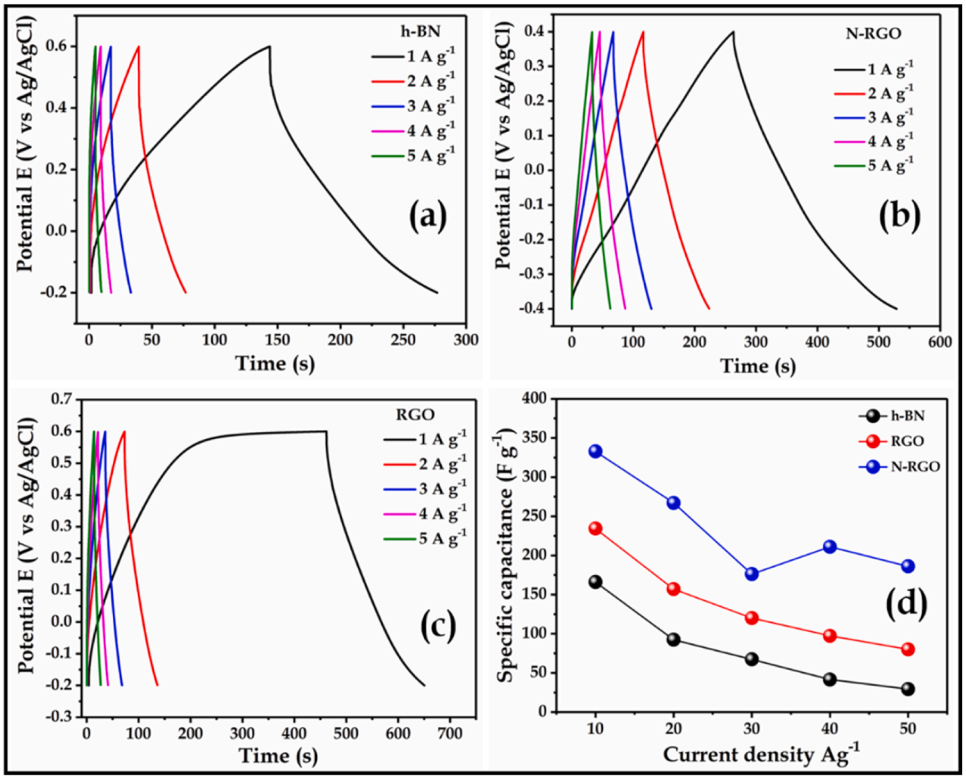

Fig. 8. (a-c) Galvanostatic charge-discharge curves of h-BN, RGO and N-RGO at current density of 1 A g^{-1} to 5 A g^{-1}. (d) Relationship between current density Vs specific capacitance for h-BN, RGO and N-RGO.

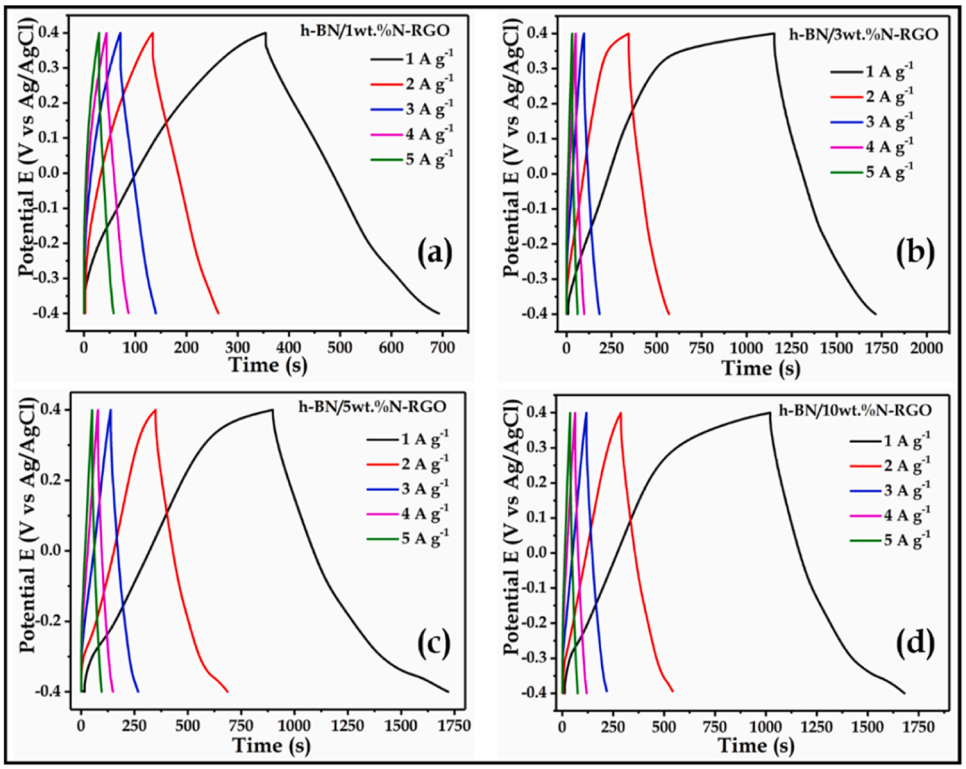

Fig. 9. (a-d) Galvanostatic charge-discharge curves of h-BN/N-RGO (1, 3, 5 and 10 % N-RGO/ h-BN) at current density of 1 A g^{-1} to 5 A g^{-1}.

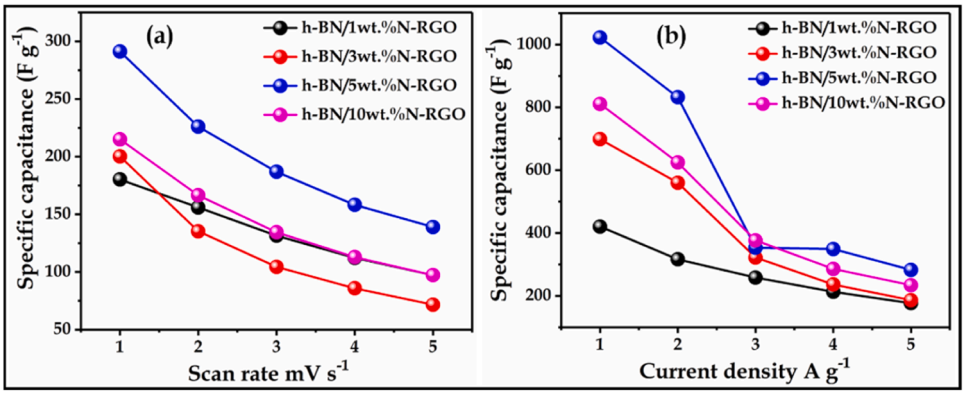

Fig. 10. (a-b) Relationship between current density Vs specific capacitance for h-BN/N-RGO (1, 3, 5 and 10 % N-RGO/ h-BN).

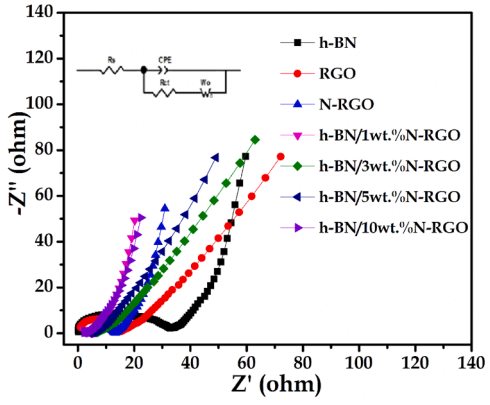

Fig. 11. Nyquist plots of h-BN, RGO, N-RGO and h-BN/N-RGO (1, 3, 5 and 10 % N-RGO/h-BN).

Here, $K_1\nu$ represents the capacitive current, and $k_2\sqrt{\nu}$ corresponds to the diffusion-controlled current. Fig. 7**b** presents the plot of the square root of scan rate ($\sqrt{\nu}$) versus the anodic peak current normalized by ($i_p/\sqrt{\nu}$). Fig. 7**c** shows 84.58 % of diffusion-controlled and 15.42 % of surface-controlled charge storage contributions at a scan rate of 10 mV s^{-1}. Finally, Fig. 7**d** illustrates the bar diagram of the capacitance contributions of the 5 % N-RGO/h-BN composite at scan rates ranging from 10 to 50 mV s^{-1}.

Fig. 8**a-c and** Fig. 9**a-d** shows the galvanostatic charge-discharge (GCD) analysis evaluates the supercapacitive performance of h-BN, RGO, N-RGO and h-BN/N-RGO (1, 3, 5 and 10 % N-RGO/ h-BN) across current densities from 1 A g^{-1} to 5 A g^{-1} within a potential window of −0.5 to 0.5 V. The non-linear triangular GCD curves indicate pseudocapacitive behavior, driven by a combination of faradaic redox reactions and capacitive charge storage. A key observation from GCD graph is the reduction in discharge time with increasing current density, attributed to enhanced OH^- ion diffusion at lower current densities, which

Table 1
Rct and Rs values of or h-BN, RGO, N-RGO and h-BN/N-RGO (1, 3, 5 and 10 % N-RGO/ h-BN).

Samples	R_{ct} (Ω)	R_s (Ω)
h-BN	33.7	0.13
RGO	13.87	0.94
N-RGO	7.15	6.1
1 % N-RGO/ h-BN	3.15	1.91
3 % N-RGO/ h-BN	2.38	4.46
5 % N-RGO/ h-BN	1.08	3.83
10 % N-RGO/ h-BN	1.64	2.27

improves specific capacitance. Fig. 8**d** and Fig. 10**b** shows comparison graph of specific capacitance vs current density for h-BN, RGO, N-RGO and h-BN/N-RGO (1, 3, 5 and 10 % N-RGO/h-BN). The calculated specific capacitance is 166, 234, 332, 420, 698, 1022 and 810 F g^{-1} for h-BN, RGO, N-RGO and h-BN/N-RGO (1, 3, 5 and 10 % N-RGO/h-BN) at the current density of 1 A g^{-1} respectively. Among the samples, 5 % N-RGO/ h-BN demonstrates superior performance with significantly higher specific capacitance values compared to h-BN, RGO, N-RGO and h-BN/N-RGO (1, 3 and 10 % N-RGO/ h-BN).

This indicates 5 % N-RGO/h-BN optimized balance of capacitive properties, and synergestic effect between N-RGO and h-BN making it the most promising candidate for high-performance supercapacitor applications. The incorporation of N-RGO with h-BN sheets enhances the overall performance by maintaining the structural integrity of the electrode material, reducing internal resistance, and improving electrolyte ion diffusion. This is reflected in the minimal IR drop observed at the start of the discharge cycle, even at higher current densities [52,53].

Fig. 11 shows Nyquist plot, which reveals the important features such as the high-frequency semicircle representing charge transfer resistance R_{ct} and the low-frequency region reflecting ion diffusion and capacitive behavior. The solution resistance (R_s) combines the intrinsic resistance of the current collector, the ionic resistance of the electrolyte, and the resistance of the electrode's active material. These factors collectively influence charge transfer efficiency and significantly affect the performance of electrochemical energy storage systems [54]. These results highlight the importance of balancing nitrogen doping and h-BN content to achieve high-performance materials with low resistance,

Table 2
Comparison of electrochemical performances for h-BN/N-RGO composites with other comparable electrodes.

Electrode (Electrolyte)	Measurement type (Operating potential window)	Specific capacitance	Energy density	Cyclic stability	Reference
PANI/h-BN composites (1 M Na_2SO_4)	2-Electrode Configuration (0.9 V)	343 F/g at 2.5 A/g	26 Wh/Kg	48 % after 100 cycles	[56]
Graphene Oxide-Thioamide polymer hybrid (1 M H_2SO_4)	2-Electrode Configuration (1.0 V)	221 F g^{-1} at 1 A g^{-1}	94.4 Wh kg^{-1}	98 % after 5000 cycles	[57]
MnO_2/CuO/Co_3O_4/rGO (1 M KOH)	2-Electrode Configuration	133.41 Fcm^{-2} at 1 A/g	41.67 $\mu Whcm^{-2}$	85.13 % after 5000 cycles	[58]
Fe3O4@onion-like carbons [3 M KOH]	2-Electrode Configuration (0.8 V)	686 F g^{-1} at 1 A/g	63.1 Wh kg^{-1}	80 % after 10,000 cycles	[59]
MoO_3-rGO (2 M KOH)	2-Electrode Configuration (0.8 V)	188 Cg^{-1} at 1 Ag^{-1}	36.78 W hkg^{-1}	87.6 % after 10,000 cycles	[60]
N, O codoped porous carbon (6 M KOH)	3-Electrode Configuration (0.5 V)	536.7 F g^{-1} at 0.5 A/g^{-1}	13.8 W h/kg	97.6 % after 15,000 cycles	[61]
Ni-MOF/GO_3/GNP (2.0 M CH_3CO_2K)	2-Electrode Configuration (1.0 V)	102.24 F/g at 1 A/g	14.02 Wh/kg	85.6 % after 20,000 cycles	[62]
NiO-rGO (2:1) (1 M NaOH)	2-Electrode Configuration (1.0 V)	27.84 F/g^{-1} at 0.1 A/g^{-1}	40.20 Wh kg^{-1}	–	[63]
Graphen/BN/Li_2TiO_3 (50 μL LIBOB)	2-Electrode Configuration (1.2 V)	1662.60 F/g at 1 A g^{-1}	124.20 Wh kg^{-1}	–	[64]
MoS_2/graphene (1 M Na_2SO_4)	2-Electrode Configuration (1.0 V)	11 mF/cm^2 at 5 mV/s	–	80 % after 10,000 cycles	[65]
h-BN/rGO (50:50) (6 M KOH)	2-Electrode Configuration (1.0 V)	90.7 F/g at 5 mV/s	–	90 % after 1000 cycles	[66]
Exfoliated h-BN/MoS_2 NCs (3 M KOH)	2-Electrode Configuration (0.6 V)	196.6C/g at 1 A/g	46.1 Wh/Kg	86 % after 2000 cycles	[67]
h-BN/C (2 M KOH)	2-Electrode Configuration (1.0 V)	17 Wh Kg^{-1}	245 W kg^{-1}	1000 cycles	[68]
Exfoliated h-BN/Bi_2S_3 NCs (3 M KOH)	2-Electrode Configuration (1.5 V)	297.5 C/g at 2 mV/s	69.8 W hkg^{-1}	92.5 % after 6000 cycles	[69]
Exfoliated h-BN/WS_2 NCs (3 M KOH)	2-Electrode Configuration (0.6 V)	142.1 C/g at 1A/g	33.37 Wh/kg	81.6 % over 10,000 cycles	[70]
h-BN/RGO composite (6 M KOH)	2-Electrode Configuration (1.4 V)	145.7 F g^{-1} at 6 A/g	39.6 Wh Kg^{-1}	89 % after 4000 cycles	[71]
h-BN/5Wt. % N-rGO nanocomposites (3 M KOH)	**3-Electrode Configuration (0.8 V)**	**1022 F g^{-1} at 1 A g^{-1}**	**–**	**–**	**Present work**
h-BN/5Wt. % N-rGO nanocomposites (3 M KOH)	**2-Electrode Configuration (1.0 V) (Coin cell)**	**86 F g^{-1} at 0.1 A g^{-1}**	**12 Wh kg^{-1}**	**88 % after 10,000 cycles**	**Present work**

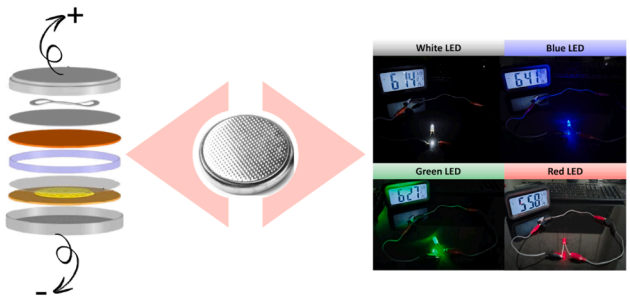

Scheme 4. Schematic representation of the symmetric coin cell architecture and its application.

excellent capacitive behavior, and outstanding stability, making N-RGO/h-BN composites ideal for advanced supercapacitor applications. The calculated solution resistance (R_s) and (R_{ct}) values for h-BN, RGO, N-RGO and h-BN/N-RGO (1, 3, 5 and 10 % N-RGO/ h-BN) are shown in Table 1.

Among the electrodes, 5 % N-RGO/h-BN exhibits the smallest semicircle in the Nyquist plot, indicating a significantly lower charge transfer resistance (R_{ct}) compared to other samples. So, the higher nitrogen doping percentages reduce R_{ct} due to increased active sites, enhancing charge transfer efficiency, while h-BN sheets improve electrolyte penetration and accessibility to these sites [55]. However, excessive nitrogen doping may lead to defects or agglomeration, increasing R_{ct} and diffusion resistance. This suggests that 5 % N-RGO/h-BN possesses superior capacitive behavior and serves as a low-resistance electrode material, making it more efficient for electrochemical applications. The evaluation of the electrochemical performance of h-BN/N-RGO composites in comparison with other comparable electrodes which shown in Table 2

3.7. Electrochemical performance analysis of coin cell supercapacitor

A symmetric supercapacitor device was fabricated using a typical CR2032 coin-cell assembly, with two 5 % N-RGO/h-BN electrodes of similar mass loading separated by porous filter paper soaked in a 3 M KOH electrolyte, all securely fixed within the coin-cell structure. Scheme 4 shows the coin cell structure and its application. Fig. 12**a-e** illustrates the symmetric coin cell configuration, of cyclic voltammetry (CV), galvanostatic charge-discharge (GCD) profiles, Nyquist plot, relationship between specific capacitance and current density for the 5 % N-RGO/h-BN electrodes.

As shown in Fig. 12**a**, the symmetric cell structure with both positive and negative electrode is 5 % N-RGO/h-BN. Fig. 12**b,** depicts the cyclic voltammetry (CV) curves of 5 % N-RGO/h-BN, showcasing quasi-rectangular shapes across scan rates of 10 mV s^{-1} to 50 mV s^{-1}, which indicates excellent capacitive behavior with the potential windows of 0–1.0 V. The CV profile retained its shape even at high scan rates, demonstrating the 5 % N-RGO/h-BN device's exceptional rate capability. Fig. 12**c** presents GCD curves at varying current densities of 0.1, 0.2, 0.3, 0.4, 0.5, 1, 2 and 3 A g^{-1}. The GCD profile of the symmetric 5 % N-RGO/h-BN coin-cell supercapacitor displayed a slightly nonlinear shape, which indicates pseudocapacitive and EDLC behavior of the electrode. Using Eq. (4), the specific capacitance values of GCD analysis were calculated as 86 F g^{-1}, 80 F g^{-1}, 68 F g^{-1}, 58 F g^{-1}, 53 F g^{-1}, 33 F g^{-1}, 19 F g^{-1}, and 14 F g^{-1} for the respective current densities.

The maximum specific capacitance of 86 F g^{-1} was achieved at a current density of 0.1 A g^{-1}, while a capacitance of 14 F g^{-1} was retained even at a high current density of 3 A g^{-1}. From this the specific capacitance was decrease with increase in current density (Fig. 12**e**). The synergy between N-RGO and h-BN sheets results in high specific capacitance, excellent energy density, and outstanding cycling stability, making these materials highly suitable for advanced supercapacitor applications. Fig. 12**d** shows Nyquist plot of 5 % N-RGO/h-BN device. The intercept on the real axis (Z') and the semicircular arc in the high-frequency region represent the equivalent series resistance (R_s) and

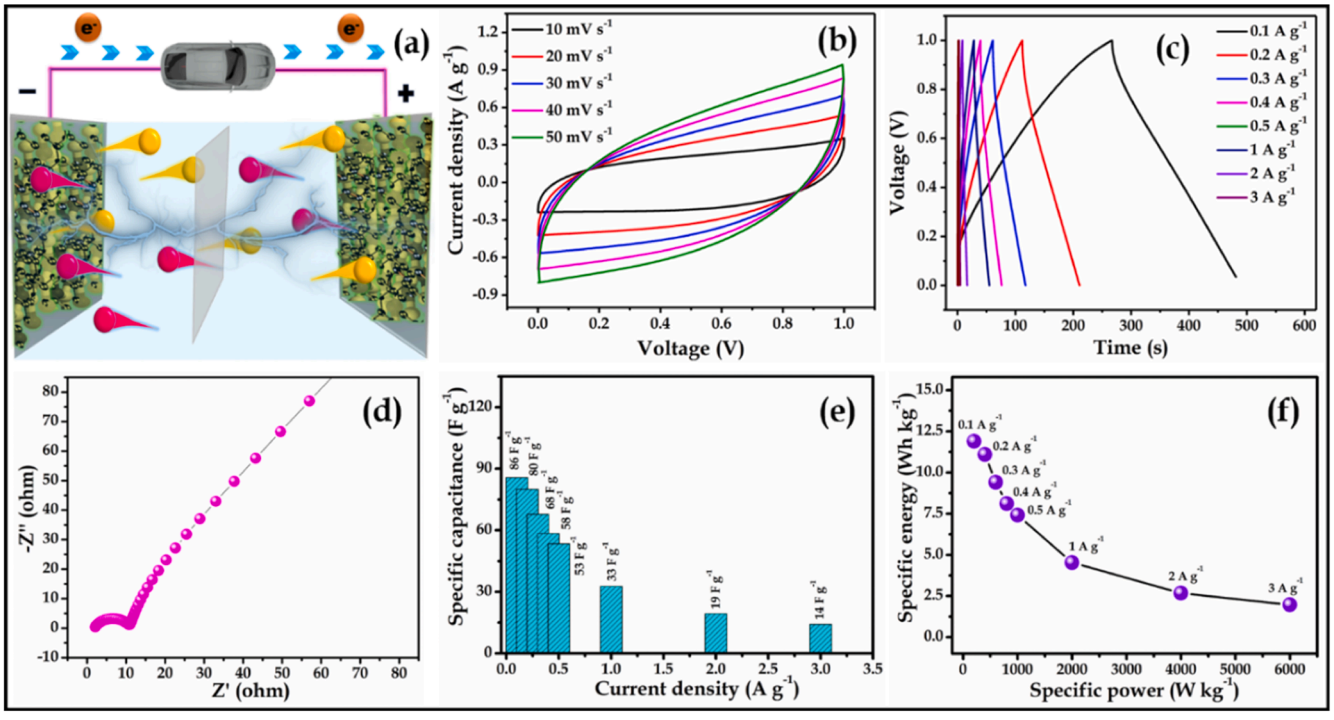

Fig. 12. Illustrates symmetric cell of 5 % N-RGO/h-BN (a) Symmetric cell structure (b) CV curves at scan rates of 10 mV s^{-1} to 50 mV s^{-1}, (c) GCD curves at current densities of 0.1 A g^{-1} to 3 A g^{-1} (d) Nyquist plot (e) comparison of specific capacitance and current density and (f) Ragone plot (specific energy vs specific power with respect to current density).

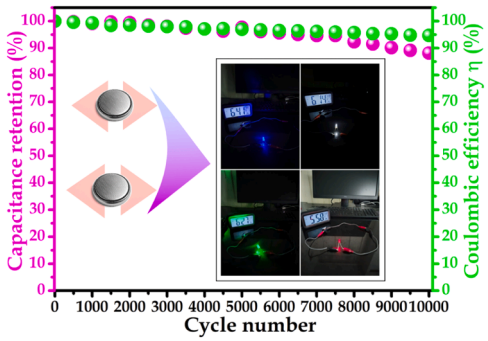

Fig. 13. Coloumbic efficiency (%) and capacitance retention (%) with respect to cycle numbers at a current density of 3 A g^{-1} (insert image: LED light with various color of blue, white, green and red).

Fig. 14. The practical application of SSSC coin cell for glowing various colour LED light illumination under room temperature condition (Temperature: 32℃; Relative Humidity: 40 %).

charge-transfer resistance (R_{ct}), with values of 1.64 Ω and 12.5 Ω which indicating low internal resistance and efficient charge transfer. The Nyquist plot's vertical alignment along the imaginary axis in the low-frequency region confirms the standard capacitive behavior of the symmetric coin-cell supercapacitor.

The energy storage capacity and power delivery performance are vital parameters for assessing the operational efficiency and practicality of a supercapacitor device. Fig. 12**f** shows Ragone plot which illustrates the specific energy and specific power characteristics, it achieved a maximum specific energy of 12 W h kg^{-1} and high specific power of 200 W kg^{-1} at 0.1 A g^{-1} current density and achieved 2 W h kg^{-1} of specific energy and 5998 W kg^{-1} of specific power at 3 A g^{-1} current density. The device exhibited excellent stability, retaining 88 % of its initial capacitance and achieving 95 % coulombic efficiency after 10,000 charge-discharge cycles at 3 A g^{-1} (Fig. 13). The 5 % performance decay was attributed to electrode material degradation from charging and discharging process, demonstrating its durability for long-term energy storage applications.

The commercial feasibility of this coin cell symmetric device was demonstrated by successfully powering various color LED bulbs, such as white, blue, green, and red. For this demonstration, three identical coin cells were connected in series, and the combined device was charged for one minute to its maximum potential of ~3 V before being discharged to power the LED bulbs. As the energy density of the cell gradually declined, a noticeable reduction in the brightness of the LED was observed, indicating the decrease in available energy over time which is shown in Fig. 14**.** This demonstration shows the potential of using these supercapacitors for practical energy storage applications, where the performance can be monitored through the power output (LED brightness) as energy is consumed.

4. Conclusions

In summary, the successful recycling of waste batteries into nitrogen-doped reduced graphene oxide (N-RGO) combined with boron nitride (BN) nanosheets, forming 2D/2D hybrid composites with significant potential for high-performance supercapacitor applications. The synthesized materials demonstrated symmetric coin cell supercapacitor shows excellent electrochemical properties, including high specific capacitance of 86 F g^{-1}, specific energy of 12 Wh kg^{-1}, and superior cycling stability with 88 % of capacitance retention up to 10,000 cycles. By integrating the high conductivity and pseudocapacitive behavior of N-RGO with the structural stability and thermal properties of BN, the hybrid composites achieved enhanced energy storage capabilities and reduced charge transfer resistance. This work underscores the potential of recycled materials in sustainable energy storage systems, offering eco-friendly and cost-effective solutions to address global energy and environmental challenges.

Ethics declaration

Not applicable

Consent to participate

Not applicable

Consent to publish

Not applicable

CRediT authorship contribution statement

Yogapriya Selvaraj: Writing – original draft, Data curation, Conceptualization. **Nandhakumar Eswaramoorthy:** Visualization, Methodology, Data curation. **Vijayakumar Elayappan:** Resources, Formal analysis. **Prem Kumar Muthusamy:** Validation, Methodology. **Anbazhagan Venkattappan:** Visualization, Formal analysis. **Kiruthika Paramasivam:** Formal analysis. **Mohamed Mussa Mtangi:** Investigation, Formal analysis. **Sambasivam Sangaraju:** Writing – review & editing, Supervision, Funding acquisition, Conceptualization.

Declaration of competing interest

The authors declare that they have no known competing financial interests or personal relationships that could have appeared to influence the work reported in this paper.

Acknowledgements

Dr. Yogapriya Selvaraj, Research Associate, Vinayaka Mission's Kirupananda Variyar Arts & Science College, Vinayaka Mission's Research Foundation Deemed to be University, Salem, and Dr. Nandhakumar Eswaramoorthy, Assistant Professor (Research), Centre for Applied Nanomaterials, Chennai Institute of Technology, Chennai, acknowledge the support for material synthesis, characterization, and

device analysis facilities. We also extend our gratitude to all the co-authors for their contributions to this research work. UAEU-AUA joint research program under grant number 12R248, and National Water and Energy Centre, United Arab Emirates University, UAE for financial support.

Supplementary materials

Supplementary material associated with this article can be found, in the online version, at doi:10.1016/j.rineng.2025.107619.

Data availability

Data will be made available on request.

References

[1] U.S. Behera, J.S. Sangwai, H.S. Byun, A comprehensive review on the recent advances in applications of nanofluids for effective utilization of renewable energy, Renew. Sustain. Energy Rev. 207 (1) (2025) 114901, https://doi.org/10.1016/j.rser.2024.114901.

[2] T. Khandaker, T. Islam, A. Nandi, M.A.A.M. Anik, M.S. Hossain, M.K. Hasan, M. S. Hossain, Biomass-derived carbon materials for sustainable energy applications: a comprehensive review, Sustain. Energy Fuels (2025), https://doi.org/10.1039/D4SE01393J.

[3] M. Goswami, S. Kumar, H. Siddiqui, V. Chauhan, N. Singh, N. Sathish, M. Ashiq, S. Kumar, Hybrid energy storage devices: li-ion and Na-ion capacitors, in: Emerging Trends in Energy Storage Systems and Industrial Applications, 1, Academic Press, 2023, pp. 223–258, https://doi.org/10.1016/B978-0-323-90521-3.00016-8.

[4] T. Prasankumar, S. Jose, P.M. Ajayan, M. Ashokkumar, Functional carbons for energy applications, Mater. Res. Bull. 142 (2021) 111425, https://doi.org/10.1016/j.materresbull.2021.111425.

[5] S. Suganya, F. Kousi, S. Sambasivam, A.M. Tighezza, K. Velsankar, S. Sudhahar, Investigations of ternary Cu-Mn-Zn oxide nanocomposites as potential electrode for hybrid supercapacitors by one-pot hydrothermal method, J. Energy Storage 109 (2025) 115181, https://doi.org/10.1016/j.est.2024.115181.

[6] G.G. Njema, R.B.O. Ouma, J.K. Kibet, A review on the recent advances in battery development and energy storage technologies, J. Renew. Energy (1) (2024) 2329261, https://doi.org/10.1155/2024/2329261.

[7] P.K. Behera, K. Gupta, M. Pattnaik, Hybrid energy storage unit fed motoring and regenerative braking control of electric vehicle drivetrain, J. Power. Sources 626 (2025) 235761, https://doi.org/10.1016/j.jpowsour.2024.235761.

[8] E.P. da Silva, V.H. Fragal, E.H. Fragal, T. Sequinel, L.F. Gorup, R. Silva, E.C. Muniz, Sustainable energy and waste management: how to transform plastic waste into carbon nanostructures for electrochemical supercapacitors, Waste Manag. 171 (2023) 71–85, https://doi.org/10.1016/j.wasman.2023.08.028.

[9] N. Noor, T. Baker, H. Lee, E. Evans, S. Angizi, J.D. Henderson, A. Rakhsha, D. Higgins, Redox-active phenanthrenequinone molecules and nitrogen-doped reduced graphene oxide as active material composites for supercapacitor applications, ACS. Omega 9 (9) (2024) 10080–10089, https://doi.org/10.1021/acsomega.3c04836.

[10] T. Bertaglia, C.M. Costa, S. Lanceros-Méndez, F.N. Crespilho, Eco-friendly, sustainable, and safe energy storage: a nature-inspired materials paradigm shift, Mater. Adv. 5 (19) (2024) 7534–7547, https://doi.org/10.1039/D4MA00363B.

[11] M. Manikandan, T. Prasankumar, E. Manikandan, E. Papanasam, K. Ramsh, S. Ramesh, Hydrothermal synthesis of rGO and MnCoS composite for enhanced supercapacitor application, Sci. Rep. 14 (2024) 25596, https://doi.org/10.1038/s41598-024-77245-5.

[12] Y. Zhu, S. Murali, W. Cai, X. Li, J.W. Suk, J.R. Potts, R.S. Ruoff, Graphene and graphene oxide: synthesis, properties, and applications, Adv. Mater. 23 (5) (2011) 673–693, https://doi.org/10.1002/adma.201000517.

[13] Y. Wang, Z. Shi, J. Yin, Facile synthesis of soluble graphene via a green reduction of graphene oxide in tea solution and its biocomposites, ACS Appl. Mater. Interfaces 3 (4) (2011) 1127–1133, https://doi.org/10.1021/am101296v.

[14] D.P. Dubal, O. Ayyad, V. Ruiz, P. Gómez-Romero, Hybrid energy storage: the merging of battery and supercapacitor chemistries, Chem. Soc. Rev. 44 (7) (2015) 1777–1790, https://doi.org/10.1039/C4CS00266K.

[15] L.L. Zhang, X.S. Zhao, Carbon-based materials as supercapacitor electrodes, Chem. Soc. Rev. 38 (9) (2009) 2520–2531, https://doi.org/10.1039/B813846J.

[16] K. Sharma, P. Kadyan, S. Grover, Heteroatom doping in bio-waste derived activated carbon for enhanced supercapacitor performance: a review, J. Energy Storage 100 (1) (2024) 113679, https://doi.org/10.1016/j.est.2024.113679.

[17] S. Roy, S. Ghosh, S. Mateti, M. Xie, A. Zavabeti, C. Xu, H. Chou, N. Syed, I.A. De Castro, J.Z. Ou, T. Daeneke, K-Z.K. Structure, Properties, and applications of two-dimensional hexagonal boron nitride, Adv. Mater. 33 (41) (2021) 2101589, https://doi.org/10.1002/adma.202101589.

[18] Y. Cai, X. Chen, Y. Xu, Y. Zhang, H. Liu, H. Zhang, J. Tang, Ti3C2Tx MXene/carbon composites for advanced supercapacitors: synthesis, progress, and perspectives, Carbon Energy 6 (2) (2024) 501, https://doi.org/10.1002/cey2.501.

[19] K. Sharma, P. Kadyan, R.K. Sharma, S. Grover, Heteroatom doping in bio-waste derived activated carbon for enhanced supercapacitor performance: a review, J Energy Storage 100 (1) (2024) 113679, https://doi.org/10.1016/j.est.2024.113679.

[20] S. Uppugalla, R. Pothu, R. Boddula, M.A. Desai, N. Al-Qahtani, Nitrogen and sulfur co-doped activated carbon nanosheets for high-performance coin cell supercapacitor device with outstanding cycle stability, Emergent Mater. 6 (4) (2023) 1167–1176, https://doi.org/10.1007/s42247-023-00503-1.

[21] S. Radhakrishnan, A. Patra, G. Manasa, M.A. Belgami, S. Mun Jeong, C.S Rout, Borocarbonitride-based emerging materials for supercapacitor applications: recent advances, challenges, and future perspectives, Adv. Sci. 11 (4) (2024) 2305325, https://doi.org/10.1002/advs.202305325.

[22] I.M. Patil, S. Kapse, H. Parse, R. Thapa, G. Andersson, B. Kakade, 2D/3D heterostructure of h-BN/reduced graphite oxide as a remarkable electrode material for supercapacitor, J. Power Sources 479 (2020) 229092, https://doi.org/10.1016/j.jpowsour.2020.229092.

[23] B. Ahmed, A. El-Ghazaly, J. Halim, J. Rosen, Electrochemical activation of commercial graphite sheets for supercapacitive applications, Electrochim. Acta 431 (2022) 140882, https://doi.org/10.1016/j.electacta.2022.140882.

[24] A. Abdisattar, M. Yeleuov, C. Daulbayev, K. Askaruly, A. Tolynbekov, A. Taurbekov, N. Prikhodko, Recent advances and challenges of current collectors for supercapacitors, Electrochem. commun. 142 (2022) 107373, https://doi.org/10.1016/j.elecom.2022.107373.

[25] Y. Selvaraj, H. Kuzhandaivel, K.S. Nallathambi, V. Elayappan, Enhanced cyclic stability of cobalt doped $Bi_{25}FeO_{40}$/$BiFeO_3$ as an electrode material for a super long-life symmetric supercapacitor device, ACS Energy Fuels 37 (12) (2023) 8624–8636, https://doi.org/10.1021/acs.energyfuels.3c00135.

[26] J. Pu, K. Zhang, Z. Wang, C. Li, K. Zhu, Y. Yao, G. Hong, Synthesis and modification of boron nitride nanomaterials for electrochemical energy storage: from theory to application, Adv. Funct. Mater. 31 (48) (2021) 2106315, https://doi.org/10.1002/adfm.202106315.

[27] J. Wang, F. Ma, M. Sun, Graphene, hexagonal boron nitride, and their heterostructures: properties and applications, RSC. Adv. 7 (27) (2017) 16801–16822, https://doi.org/10.1021/jp904246j.

[28] R. Gao, L. Yin, C. Wang, Y. Qi, N. Lun, L. Zhang, Y.X. Liu, L. Kang, X. Wang, High-yield synthesis of boron nitride nanosheets with strong ultraviolet cathodoluminescence emission, J. Phy. Chem. C 113 (34) (2009) 15160–15165, https://doi.org/10.1021/jp904246j.

[29] B. Sanjay, N. Phong, C. Songwei, D. Rousan, B. Vikas, Large-area, transfer-free, oxide-assisted synthesis of hexagonal boron nitride films and their heterostructures with MoS2 and WS2, J. Am. Chem. Soc. 137 (40) (2015) 13060–13065, https://doi.org/10.1021/jacs.5b07739.

[30] J. Wang, F. Ma, W. Liang, R. Wang, M. Sun, Optical, photonic and optoelectronic properties of graphene, h-BN and their hybrid materials, Nanophoto 6 (5) (2017) 943–976, https://doi.org/10.1515/nanoph-2017-0015.

[31] M. Ikram, A. Raza, M. Imran, A. Ul-Hamid, A. Shahbaz, S. Ali, Hydrothermal synthesis of silver decorated reduced graphene oxide (rGO) nanoflakes with effective photocatalytic activity for wastewater treatment, Nanoscale Res. Lett. 15 (1) (2020) 1–11, https://doi.org/10.1186/s11671-020-03323-y.

[32] V. Ramar, K. Balasubramanian, Charge transfer induced tunable bandgap and enhanced saturable absorption behavior in rGO/WO3 composites, Appl. Phys. A 124 (1) (2018) 1–11, https://doi.org/10.1007/s00339-018-2191-3.

[33] T. Soltani, B.K. Lee, A benign ultrasonic route to reduced graphene oxide from pristine graphite, J. Colloid Interface Sci. 486 (1) (2017) 337–343, https://doi.org/10.1016/j.jcis.2016.09.075.

[34] M. Ikram, A. Raza, M. Imran, A. Ul-Hamid, A. Shahbaz, S. Ali, Hydrothermal synthesis of silver decorated reduced graphene oxide (rGO) nanoflakes with effective photocatalytic activity for wastewater treatment, Nanoscale Res. Lett. 15 (1) (2020) 1–11, https://doi.org/10.1186/s11671-020-03323-y.

[35] B. Matović, J. Luković, M. Nikolić, B. Babić, N. Stanković, B. Jokić, B. Jelenković, Synthesis and characterization of nanocrystaline hexagonal boron nitride powders: XRD and luminescence properties, Ceram. Int. 42 (15) (2016) 16655–16658, https://doi.org/10.1016/j.ceramint.2016.07.096.

[36] S. Shaybanizadeh, A.N. Chermahini, Fabricating boron nitride nanosheets from hexagonal BN in water solution by a combined sonication and thermal-assisted hydrolysis method, Ceram. Int. 47 (8) (2021) 11122–11128, https://doi.org/10.1016/j.ceramint.2020.12.236, d.

[37] P.K. Rastogi, K.R. Sahoo, P. Thakur, R. Sharma, S. Bawari, R. Podila, T. N. Narayanan, Graphene–h-BN non-van der Waals vertical heterostructures for four-electron oxygen reduction reaction, Phy. Chem. Chem. Phy. 21 (7) (2019) 3942–3953, https://doi.org/10.1039/C8CP06155F.

[38] K. Makgopa, M.S. Ratsoma, K. Raju, L.F. Mabena, K.D. Modibane, One-step hydrothermal synthesis of nitrogen-doped reduced graphene oxide/hausmannite manganese oxide for symmetric and asymmetric pseudocapacitors, ACS. Omega 6 (47) (2021) 31421–31434, https://doi.org/10.1021/acsomega.1c02302. Dd.

[39] S. Roy Chowdhury, T. Maiyalagan, CuCo2S4@ B, N-doped reduced graphene oxide hybrid as a bifunctional electrocatalyst for oxygen reduction and evolution reactions, ACS. Omega 7 (23) (2022) 19183–19192, https://doi.org/10.1021/acsomega.2c00183.

[40] K. Yang, X. Yang, Z. Liu, K. Li, Y. Yue, R. Zhang, F. Wang, X. Shi, J. Yuan, N. Liu, G. Wang, Vertically aligned boron nitride nanosheets films for superior electronic cooling, ACS Appl. Mater. Interfaces 15 (23) (2023) 28536–28545, https://doi.org/10.1021/acsami.3c04126.

[41] Y. Mussa, F. Ahmed, M. Arsalan, E. Alsharaeh, Two dimensional (2D) reduced graphene oxide (RGO)/hexagonal boron nitride (h-BN) based nanocomposites as anodes for high temperature rechargeable lithium-ion batteries, Sci. Rep. 10 (1) (2020) 1882, https://doi.org/10.1038/s41598-020-58439-z.

[42] Z.S. Wu, W. Ren, L. Xu, F. Li, H.M. Cheng, Doped graphene sheets as anode materials with superhigh rate and large capacity for lithium ion batteries, ACS. Nano 5 (7) (2011) 5463–5471, https://doi.org/10.1021/nn2006249. D.
[43] B. Gupta, N. Kumar, K. Panda, V. Kanan, S. Joshi, I. Visoly-Fisher, Role of oxygen functional groups in reduced graphene oxide for lubrication, Sci. Rep. 7 (1) (2017) 45030, https://doi.org/10.1038/srep45030.
[44] T.W. Tang, R. Ritika, M. Tamtaji, H. Liu, Y. Hu, Z. Liu, P.R. Galligan, M. Xu, J. Shen, J. Wang, J. You, Structured-defect engineering of hexagonal boron nitride for identified visible single-photon emitters, ACS. Nano 19 (9) (2025) 8509–8519, https://doi.org/10.1021/acsnano.4c11413.
[45] X. Yu, S. Yun, J.S. Yeon, P. Bhattacharya, L. Wang, S.W. Lee, X. Hu, H.S. Park, Emergent pseudocapacitance of 2D nanomaterials, Adv. Energy Mater. 8 (13) (2018) 1702930, https://doi.org/10.1002/aenm.201702930.
[46] A. Krittayavathananon, P. Iamprasertkun, M. Sawangphruk, Enhancing the charge-storage performance of N-doped reduced graphene oxide aerogel supercapacitors by adsorption of the cationic electrolytes with single-stand deoxyribonucleic acid, Carbon. N. Y. 109 (1) (2016) 314–320, https://doi.org/10.1016/j.carbon.2016.08.018.
[47] S. Saha, W. Jang, N.C. Murmu, H. Koo, T. Kuila, Optimization of chemi-adsorption, EDLC, and redox capacitance through electro-precipitation synthesis of Fe3O4/NiO@ rGO/h-BN for the development of hybrid supercapacitor, ChemistrySelect. 4 (2) (2019) 589–599, https://doi.org/10.1002/slct.201803611.
[48] M. Skorupska, A. Ilnicka, J.P. Lukaszewicz, The effect of nitrogen species on the catalytic properties of N-doped graphene, Sci. Rep. 11 (1) (2021) 23970, https://doi.org/10.1038/s41598-021-03403-8.
[49] W. Pholauyphon, P. Charoen-amornkitt, T. Suzuki, S. Tsushima, Guidelines for supercapacitor electrochemical analysis: a comprehensive review of methodologies for finding charge storage mechanisms, J. Enery Storage 98 (1) (2024) 112833, https://doi.org/10.1016/j.est.2024.112833.
[50] C.V.M. Gopi, S. Alzahmi, M.Y. Al-Haik, Y.A. Kumar, F. Hamed, Y. Haik, I. M. Obaidat, Recent advances in pseudocapacitive electrode materials for high energy density aqueous supercapacitors: combining transition metal oxides with carbon nanomaterials, Mat. Today Sustain. 28 (1) (2024) 100981, https://doi.org/10.1016/j.mtsust.2024.100981.
[51] Y. Kumar, S. Rawal, B. Joshi, S.A. Hashmi, Background, fundamental understanding and progress in electrochemical capacitors, J. Sol. St. Electrochem. 23 (1) (2019) 667–692, https://doi.org/10.1007/s10008-018-4160-3.
[52] N. Althubaiti, Y. Mussa, C.S. Bongu, Z. Bayhan, M. Arsalan, A. Soliman, E. Alsharaeh, Reduced graphene oxide/hexagonal boron nitride-based composite as a positive electrode in asymmetric supercapacitors, J. Mater. Sci. 57 (30) (2022) 14371–14385, https://doi.org/10.1007/s10853-022-07525-w.
[53] S. Saha, M. Jana, P. Samanta, N.C. Murmu, N.H. Kim, T. Kuila, J.H. Lee, Investigation of band structure and electrochemical properties of h-BN/rGO composites for asymmetric supercapacitor applications, Mater. Chem. Phy. 190 (1) (2017) 153–165, https://doi.org/10.1016/j.matchemphys.2017.01.025.
[54] M. Liu, J.C. Liu, Y. Zhang, X. Han, H. Li, Z.H. Huang, T. Ma, Current collectors for supercapacitors: objectives, modification methods and challenges, Chem. Electro. Chem. 12 (1) (2024) 202400513, https://doi.org/10.1002/celc.202400513.
[55] L. Gao, T. Sheng, H. Ren, T.X. Liu, M. Birkett, S.W. Joo, J. Huang, Boron nitride wrapped N-doped carbon nanosheet as a host for advanced lithium-sulfur battery, Appl. Surf. Sci. 597 (30) (2022) 153687, https://doi.org/10.1016/j.apsusc.2022.153687.
[56] M.M. Rahman, M.R. Hossen, I. Alam, M.H. Rahman, O. Faruk, M. Nurbas, M. M. Rahman, M.M.R. Khan, Synthesis of hexagonal boron nitride based PANI/h-BN and PANI-PPy/h-BN nanocomposites for efficient supercapacitors, J. Alloys Compd. 947 (1) (2023) 169471, https://doi.org/10.1016/j.jallcom.2023.169471.
[57] W. Czepa, S. Witomska, P. Samorì, A. Ciesielski, A graphene oxide–Thioamide polymer hybrid for high-performance supercapacitor electrodes, Small. Sci. 3 (5) (2023) 2300013, https://doi.org/10.1002/smsc.202300013.
[58] P.J.S. Jennifer, S. Muthupandi, J. Madhavan, A.P. Prabhu, A.A. Steffy, M.V.A. Raj, Fabricating high-performance symmetric coin cell supercapacitor using MnO2/CuO/Co3O4 decorated on rGO sheets as electrode material, Diam. Rel. Mater. 1 (1) (2024) 111285, https://doi.org/10.1016/j.diamond.2024.111285.
[59] X. Jiao, B. Li, J. Wang, Y. Fan, Y. Ma, Z. Yuan, C. Zhang, Size-controllable synthesis of covalently interconnected few-shelled Fe3O4@ onion-like carbons for high-performance asymmetric supercapacitors, Carbon. N. Y. 203 (1) (2023) 261–272, https://doi.org/10.1016/j.carbon.2022.11.053.
[60] G.V. Dilwale, G. Piao, H. Kim, A.C. Pawar, Z. Said, R.K. Nimat, J.M. Kim, R. N. Bulakhe, Chemical route synthesis of nanohybrid MoO3-rGO for high-performance hybrid supercapacitors, J. Energy Storage 9 (1) (2024) 1112050, https://doi.org/10.1016/j.est.2024.112050.
[61] T. Feng, S. Wang, Y. Hua, P. Zhou, G. Liu, K. Ji, Z. Lin, S. Shi, X. Jiang, R. Zhang, Synthesis of biomass-derived N, O-codoped hierarchical porous carbon with large surface area for high-performance supercapacitor, J. Energy Storage 44 (1) (2021) 103286, https://doi.org/10.1016/j.est.2021.103286.
[62] I. Ibrahim, S. Zheng, C.Y. Foo, N.M. Huang, H.N. Lim, Hierarchical nickel-based metal-organic framework/graphene oxide incorporated graphene nanoplatelet electrode with exceptional cycling stability for coin cell and pouch cell supercapacitors, J. Energy Storage 43 (1) (2021) 103304, https://doi.org/10.1016/j.est.2021.103304.
[63] R.I.M. Vitto, M.T. Natividad, S.T. Palisoc, High-performance and low-cost coin-cell supercapacitors based on waste graphite from spent dry-cell batteries, J. Power Sources 582 (1) (2023) 233547, https://doi.org/10.1016/j.jpowsour.2023.233547.
[64] R. Mendoza-Jiménez, J. Oliva, A.I. Mtz-Enriquez, N.O. Etafo, V. Rodriguez-Gonzalez, Enhancement of capacitance and widening of the operating voltage window of flexible supercapacitors by adding Li2TiO3/BN on their electrodes, Ceram. Int. 49 (12) (2023) 20980–20988, https://doi.org/10.1016/j.ceramint.2023.03.232.
[65] M.A. Bissett, I.A. Kinloch, R.A. Dryfe, Characterization of MoS2–graphene composites for high-performance coin cell supercapacitors, ACS Appl. Mater. Interfaces. 7 (31) (2015) 17388–17398, https://doi.org/10.1021/acsami.5b04672.
[66] N. Althubaiti, Y. Mussa, C.S. Bongu, Z. Bayhan, M. Arsalan, A. Soliman, E. Alsharaeh, Reduced graphene oxide/hexagonal boron nitride-based composite as a positive electrode in asymmetric supercapacitors, J. Mater. Sci. 57 (30) (2022) 14371–14385, https://doi.org/10.1007/s10853-022-07525-w.
[67] K. Dhamodharan, A.K. Singh, Coupled interaction of exfoliated hexagonal boron nitride nanosheets decorated with MoS2 nanoflowers to enrich electrochemical activities for hybrid supercapacitor applications, J. Alloys. Compd. 997 (1) (2024) 174732, https://doi.org/10.1016/j.jallcom.2024.174732.
[68] T. Li, X. Jiao, T. You, F. Dai, P. Zhang, F. Yu, L. Hu, L. Ding, L. Zhang, Z. Wen, Y. Wu, Hexagonal boron nitride nanosheet/carbon nanocomposite as a high-performance cathode material towards aqueous asymmetric supercapacitors, Ceram. Int. 45 (4) (2019) 4283–4289, https://doi.org/10.1016/j.ceramint.2018.11.101.
[69] D. Krishnamoorthy, A.K. Singh, Investigating the exfoliated hexagonal boron nitride nanosheets embedded on Bi2S3 nanorods designed as a positive electrode for hybrid supercapacitors, Energy Fuels 38 (21) (2024) 21468–21481, https://doi.org/10.1021/acs.energyfuels.4c03282.
[70] K. Dhamodharan, A.K. Singh, Two-dimensional exfoliated hexagonal boron nitride-WS2 nanosheets emerge as an efficient positive electrode for high performance hybrid supercapacitor applications, Diam. Relat. Mater. (1) (2025) 111976, https://doi.org/10.1016/j.diamond.2025.111976.
[71] S. Saha, M. Jana, P. Khanra, P. Samanta, H. Koo, N.C. Murmu, T. Kuila, Band gap engineering of boron nitride by graphene and its application as positive electrode material in asymmetric supercapacitor device, ACS. Appl. Mater. Interfaces. 7 (26) (2015) 14211–14222, https://doi.org/10.1021/acsami.5b03562.